**6692** *Inorg. Chem.* **2009**, *48*, 6692–6712
DOI: 10.1021/ic900652y

Inorganic Chemistry
Article

# Lanthanide Complexes of Triethylenetetramine Tetra-, Penta-, and Hexaacetamide Ligands as Paramagnetic Chemical Exchange-Dependent Saturation Transfer Contrast Agents for Magnetic Resonance Imaging: Nona- versus Decadentate Coordination

**Dirk Burdinski,*,† Jeroen A. Pikkemaat,‡ Johan Lub,† Peter de Peinder,§ Lidia Nieto Garrido,† and Thomas Weyhermüller∥**

†*Department of Biomolecular Engineering and* ‡*Department of Materials Analysis, Philips Research Europe, High Tech Campus 11, 5656 AE Eindhoven, The Netherlands,* §*VibSpec, Haaftenlaan 28, 4006 XL Tiel, The Netherlands, and* ∥*Max-Planck-Institut für Bioanorganische Chemie, Stiftstrasse 34-36, 45470 Mülheim an der Ruhr, Germany*

Received April 2, 2009

The solid state and solution structure of a series of lanthanide complexes of the decadentate ligand triethylenetetramine-*N*,*N*,*N*′,*N*″,*N*‴,*N*⁗-hexaacetamide, (ttham), its two decadentate derivatives di-*tert*-butyl *N*,*N*,*N*‴,*N*⁗-tetra(carbamoylmethyl)-triethylenetetramine-*N*′,*N*″-diacetate ($Bu_2$ttha-tm) and *N*,*N*,*N*‴,*N*⁗-tetra(carbamoylmethyl)-triethylenetetramine-*N*′,*N*″-diacetic acid ($H_2$ttha-tm), and its two nonadentate derivatives *N*-benzyl-triethylenetetramine-*N*,*N*′,*N*″,*N*‴,*N*⁗-pentaacetamide (1bttpam) and *N*′-benzyl-triethylenetetramine-*N*,*N*,*N*″,*N*‴,*N*⁗-pentaacetamide (4bttpam) have been investigated by infrared and Raman spectroscopy, X-ray crystallography, cyclovoltammetry, and NMR spectroscopy. In these mononuclear lanthanide complexes, the first coordination sphere is generally saturated by four amine nitrogens of the triethylenetetramine ligand backbone and five or six carbonyl oxygen atoms of the pendent amide or acetate donor groups. In the $[Ln(ttham)]^{3+}$ complex series, a switch from a decadentate to a nonadentate coordination occurs between $[Er(ttham)]^{3+}$ and $[Tm(ttham)]^{3+}$. This switch in coordination mode, which is caused by decreasing metal ion radii going from lanthanum to lutetium (lanthanide contraction), has no significant effect on the $T_1$-relaxivity of these complexes. It is shown that the $T_1$-relaxivity is dominated by second coordination sphere interactions, with an ascendant contribution of the classical dipolar relaxation mechanism for the earlier (Ce−Sm) and very late (Tm, Yb) lanthanides, and a prevailing Curie relaxation mechanism for most of the remaining paramagnetic lanthanide ions. In chemical exchange-dependent saturation transfer (CEST) $^1$H NMR experiments, most of the above complexes exhibit multiple strong CEST peaks of the paramagnetically shifted amide protons spread over a >100 ppm chemical shift range. The effective CEST effect of the studied thulium complexes strongly depends on temperature and pH. The pH at which the CEST effect maximizes (generally between pH 7 and 8) is determined by the overall charge of the complex. Depending on the used saturation frequency offset, the temperature-dependence varies between the extremes of strongly linearly dependent and fully independent in the case of $[Tm(ttham)]^{3+}$. In combination with the strong pH-dependence of the CEST effect at the latter frequency offset, this complex is highly suitable for simultaneous temperature and pH mapping using magnetic resonance imaging.

## Introduction

A new class of magnetic resonance imaging (MRI) contrast agents (CAs) that is based on the chemical exchange-dependent saturation transfer (CEST) effect has attracted much attention in recent years.[1−4] CEST agents are conceptually different from classical gadolinium-based $T_1$ CAs, which locally shorten the relaxation time of bulk water protons to generate contrast in magnetic resonance (MR) images essentially without external control.[5−7] In contrast, in the presence

*To whom correspondence should be addressed. E-mail: dirk.burdinski@philips.com.

(1) Aime, S.; Geninatti Crich, S.; Gianolio, E.; Giovenzana, G. B.; Tei, L.; Terreno, E. *Coord. Chem. Rev*. **2006**, *250*, 1562–1579.
(2) Zhou, J.; van Zijl, P. C. M. *Prog. Nucl. Magn. Reson. Spectrosc*. **2006**, *48*, 109–136.
(3) Sherry, A. D.; Woods, M. *Annu. Rev. Biomed. Eng*. **2008**, *10*, 391–411.
(4) Delli Castelli, D.; Gianolio, E.; Geninatti Crich, S.; Terreno, E.; Aime, S. *Coord. Chem. Rev*. **2008**, *252*, 2424–2443.
(5) Aime, S.; Botta, M.; Terreno, E. Gd(III)-based contrast agents for MRI. In *Advanced Inorganic Chemistry*; Elsevier: San Diego, 2005; Vol. 57, pp 173−237.
(6) Caravan, P.; Ellison, J. J.; McMurry, T. J.; Lauffer, R. B. *Chem. Rev*. **1999**, *99*, 2293–2352.
(7) Tóth, É.; Helm, L.; Merbach, A. E. Metal Complexes as MRI Contrast Enhancement Agents. In *Comprehensive Coordination Chemistry II*; Elsevier: Amsterdam, **2004**; Vol. *9*, pp 841−-881.

 Published on Web 06/09/2009 

of a CEST agent the signal intensity of the bulk water protons can be altered at will. Control over the local signal intensity is gained by selectively saturating, with a weak, multisecond radio frequency (RF) pulse, the resonance frequency of mildly acidic protons of the CEST agent, which are in an intermediately fast exchange equilibrium with the bulk water. The magnitude of the magnetization transfer to the bulk water, the CEST effect, and hence the extent of $^1$H MRI signal attenuation, is usually calculated according to eq 1.[2]

$$\%\mathrm{CEST} = (M_0 - M_S)/M_\infty \cdot 100\% \qquad (1)$$

$M_S$, $M_0$, and $M_\infty$ are MR intensities measured immediately after an RF saturation pulse has been applied at the resonance frequency of the CA's exchangeable protons ($\omega_S$), at the respective frequency on the opposite side of the bulk water signal ($\omega_0$) to correct for non-selective saturation, most prominently direct water saturation, and at a second reference frequency, at which the MR signal is not affected by magnetization transfer effects ($\omega_\infty$). The proximity of suitable, mildly acidic protons, typically those of organic amide groups, to a paramagnetic lanthanide ion in paraCEST agents causes the resonances of the exchangeable protons to be significantly shifted from the bulk water resonance signal. This, in general, allows for application of the saturation pulse and detection of the associated CEST effect with a high selectivity.[8,9]

Since the CEST-based contrast enhancement can be controlled by the operator, the information obtained with this specific technique can be immediately correlated with an unenhanced reference image, which can be measured without time delay. This property is of particular interest for molecular imaging applications. In this context, strategies have already been devised to modulate the CEST effect in response to physiologically meaningful parameters,[10] such as pH,[11−13] temperature,[14] metabolite concentration,[15] or enzyme activity.[16]

The sensitivity of CEST agents, an important aspect of their applicability in molecular imaging, has successfully been improved by increasing the number of CEST-active groups per agent utilizing dendritic, polymeric, or nanoparticle-based agents carrying a large number of small molecule paraCEST reporter units.[11,17−20] In a complementary approach, we designed a series of chelate ligands that allow for a maximum number of CEST-active amide groups per lanthanide ion in small molecule paraCEST complexes, which could then be linked easily to a larger carrier.[21,22] The ytterbium complexes of the ligands ttham, 1bttpam, and 4bttpam (Chart 1) were found to exhibit a nonadentate coordination geometry in solution.[23] Since the ligand ttham is potentially decadentate, the complex $[Yb(ttham)]^{3+}$ is coordinatively frustrated. It was concluded that because of steric constraints, in addition to the four backbone nitrogen atoms and the two central amide groups, only three of the four symmetry-equivalent terminal acetamide donors can coordi-

**Chart 1**

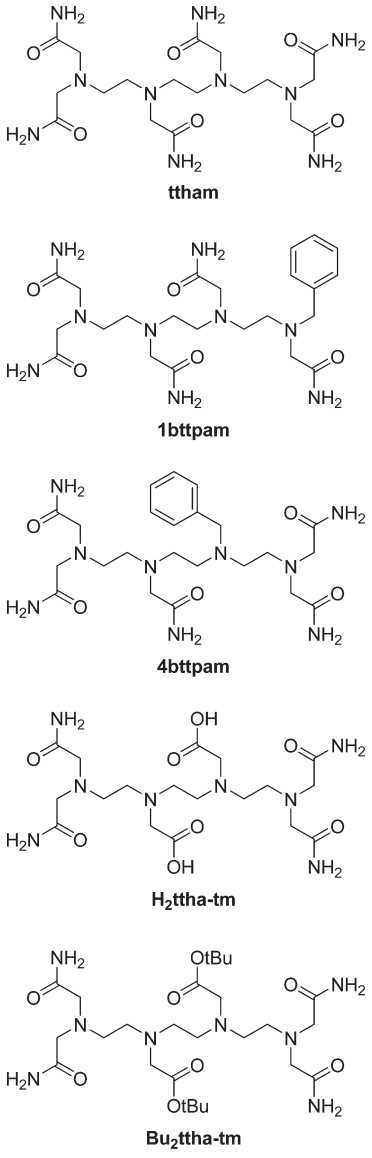


(8) Woods, M.; Woessner, D. E.; Sherry, A. D. *Chem. Soc. Rev.* **2006**, *35*, 500–511.
(9) Zhang, S.; Merritt, M.; Woessner, D. E.; Lenkinski, R. E.; Sherry, A. D. *Acc. Chem. Res.* **2003**, *36*, 783–790.
(10) Yoo, B.; Pagel, M. D. *Frontiers Biosci.* **2008**, *13*, 1733–1752.
(11) Pikkemaat, J. A.; Wegh, R. T.; Lamerichs, R.; van de Molengraaf, R. A.; Langereis, S.; Burdinski, D.; Raymond, A. Y. F.; Janssen, H. M.; de Waal, B. F. M.; Willard, N. P.; Meijer, E. W.; Grüll, H. *Contrast Media Mol. Imaging* **2007**, *2*, 229–239.
(12) Aime, S.; Delli Castelli, D.; Terreno, E. *Angew. Chem., Int. Ed.* **2002**, *41*, 4334–4336.
(13) Ward, K. M.; Balaban, R. S. *Magn. Reson. Med.* **2000**, *44*, 799–802.
(14) Zhang, S.; Malloy, C. R.; Sherry, A. D. *J. Am. Chem. Soc.* **2005**, *127*, 17572–17573.
(15) Aime, S.; Delli Castelli, D.; Fedeli, F.; Terreno, E. *J. Am. Chem. Soc.* **2002**, *124*, 9364–9365.
(16) Yoo, B.; Raam, M. S.; Rosenblum, R. M.; Pagel, M. D. *Contrast Media Mol. Imaging* **2007**, *2*, 189–198.
(17) Aime, S.; Delli Castelli, D.; Terreno, E. *Angew. Chem., Int. Ed.* **2003**, *42*, 4527–4529.
(18) Goffeney, N.; Bulte, J. W. M.; Duyn, J.; Bryant, L. H.Jr.; van Zijl, P. C. M. *J. Am. Chem. Soc.* **2001**, *123*, 8628–8629.
(19) Winter, P. M.; Cai, K.; Chen, J.; Adair, C. R.; Kiefer, G. E.; Athey, P. S.; Gaffney, P. J.; Buff, C. E.; Robertson, J. D.; Caruthers, S. D.; Wickline, S. A.; Lanza, G. M. *Magn. Reson. Med.* **2006**, *56*, 1384–1388.
(20) Wu, Y.; Zhou, Y.; Ouari, O.; Woods, M.; Zhao, P.; Soesbe, T. C.; Kiefer, G. E.; Sherry, A. D. *J. Am. Chem. Soc.* **2008**, *130*, 13854–13855.
(21) Burdinski, D.; Lub, J.; Pikkemaat, J. A.; Grüll, H.; Nieto Garrido, L.; Girard, S. G.; Moreno Jalón, D.; Weyhermüller, T. *J. Biol. Inorg. Chem.* **2007**, *17*, S17–S17.
(22) Burdinski, D.; Lub, J.; Pikkemaat, J. A.; Wegh, R. T.; Grüll, H.; Nieto Garrido, L.; Girard, S. G.; Martial, S.; Del Pozo Ochoa, C.; Moreno Jalón, D.; Weyhermüller, T. *Proc. Int. Soc. Magn. Reson. Med.* **2007**, *15*, 1182–1182.
(23) Burdinski, D.; Lub, J.; Pikkemaat, J. A.; Moreno Jalón, D.; Martial, S.; Del Pozo Ochoa, C. *Dalton Trans.* **2008**, 4138–4151.

nate simultaneously to the ytterbium ion, and the dangling fourth acetamide exchanges quickly with the other three. In solution, the low symmetry of these complexes appeared to prevent the realization of very high CEST effects.

The aim of this study was to interrogate the coordination properties of the ttham ligand with the remaining lanthanide ions. Taking into consideration the lanthanide contraction effect, we expected that upon moving to the earlier lanthanides, a decadentate, more symmetric coordination geometry would be achievable promising improved CEST properties. In addition, two new, decadentate ligands, di-*tert*-butyl *N*,*N*,*N*‴,*N*‴-tetra(carbamoylmethyl)-triethylenetetramine-*N*′,*N*″-diacetate ($Bu_2$ttha-tm) and *N*,*N*,*N*‴,*N*‴-tetra(carbamoylmethyl)-triethylenetetramine-*N*′,*N*″-diacetic acid ($H_2$ttha-tm, Chart 1), were prepared to probe the influence of the donor type and charge on the coordination mode of the ligand and the CEST properties of the resulting lanthanide complexes.

## Experimental Section

All solvents were obtained from Merck. 4-Morpholinepropanesulfonic acid (MOPS, 99.5%) and all other commercial chemicals were purchased from Sigma-Aldrich in the highest available quality. NMR spectra for structure verification were recorded for solutions in deuterated solvents (dichloromethane, chloroform, or dimethylsulfoxide) using a Bruker DPX300 spectrometer. MALDI-TOF mass spectra were recorded on a Voyager−DE Pro (PerSeptive Biosystems, Perkin-Elmer) mass spectrometer using α-cyano-4-hydroxycinnamic acid as a matrix and a positive reflector mode detection method. ESI mass spectra were recorded on an LCQ Deca XP Max (Thermo Finnigan) mass spectrometer using an $H_2O/CH_3CN$ (1:1) mixture as the solvent and an injection rate of 0.05 mL $min^{-1}$. High-resolution ESI (HR-ESI) mass spectra of samples dissolved in Milli-Q water were recorded via direct infusion on an Agilent ESI-TOF mass spectrometer, measuring in the positive ion mode. MS peak assignments were made based on exact mass calculations and peak pattern simulations using the software package ChemBioDraw Ultra 11.0 (CambridgeSoft).

**Elemental Analysis.** The chloride content was determined by ion chromatography of aqueous sample solutions against calibration standards using a Dionex ICS3000 ion chromatograph with conductivity detection. The lanthanide content was determined by inductively coupled plasma-atomic emission spectroscopy (ICP-AES). In preparation of ICP-AES analysis, material samples were heated with hydrochloric acid at 128 °C for 2 h. Then a small amount of 70% perchloric acid was added, and the temperature was raised to 180 °C for 1 d. The obtained solutions were cooled and diluted with water to a known volume. C, H, N analyses were performed by means of conductivity measurement after combustion of the material with a plug of oxygen and separation of the combustion gases.

***Caution!*** *Although we experienced no difficulties, the unpredictable behavior of perchloric acid and perchlorate salts necessitates extreme caution in their handling.*

**Infrared and Raman Spectroscopy.** FT-IR spectra were obtained on an ATI Mattson Genesis II spectrometer by Attenuated Total Reflection (ATR, SplitPea, Harrick Scientific). Spectra were recorded at 1 $cm^{-1}$ resolution, and 4 scans were accumulated. Reported absorption bands were sharp and exhibited medium to strong intensity, unless noted otherwise (br = broad). FT-Raman spectra were obtained with a Bruker Equinox 55 spectrometer combined with a Bruker FRA 106/S module equipped with a Ge detector (liquid $N_2$ cooling) attached. Spectra were recorded with a 1064 nm laser at 250 mW laser power, and 100 scans at 4 $cm^{-1}$ resolution were accumulated. PCA modeling was carried out with the PLS Toolbox (Eigenvector Research, Inc.) for MatLab (The MathWorks, Inc.). Prior to modeling, the IR and Raman spectra were preprocessed by applying a baseline correction, followed by Multiplicative Signal Correction (MSC) and Mean Centering (MC) of the selected regions.

**X-ray Crystallographic Data Collection and Refinement of the Structures.** Colorless single crystals of [Eu(ttham)]$(ClO_4)_3 \cdot 3H_2O$, [Eu(1bttpam)]$(ClO_4)_3 \cdot 3.65H_2O$, and [Tm(1bttpam)]$(ClO_4)_3 \cdot 4H_2O$ were coated with perfluoropolyether, picked up with nylon loops, and immediately mounted in the nitrogen cold stream of a Bruker-Nonius KappaCCD diffractometer equipped with a Mo-target rotating-anode X-ray source (Mo Kα radiation, $\lambda = 0.71073$ Å) and a graphite monochromator. Final cell constants were obtained from least-squares fits of all measured reflections. Intensity data of the 1bttpam complexes were corrected for absorption using intensities of redundant reflections with the program SADABS.[24] A Gaussian absorption correction was used in case of [Eu(ttham)]$(ClO_4)_3$. The structures were readily solved by Patterson methods and subsequent difference Fourier techniques. The Siemens ShelXTL[25] software package was used for solution and artwork of the structures; ShelXL97[26] was used for refinement. All non-hydrogen atoms were anisotropically refined, and hydrogen atoms bound to carbon and nitrogen atoms were placed at calculated positions and refined as riding atoms with isotropic displacement parameters. Hydrogen atom positions of virtually all water molecules of crystallization could not be reliably located and were therefore not included in the refinement. All three structures suffer from severe disorder of perchlorate anions and water molecules of crystallization.

Two perchlorate anions of [Tm(1bttpam)]$(ClO_4)_3 \cdot 4H_2O$ were found to be disordered and were split on three positions in case of the anion containing Cl(80) and two positions in case of Cl(90), respectively. The occupation ratio refined to about 0.54:0.28:0.18 for Cl(80) and 0.54:0.46 in case of the anion containing Cl(90). Water molecules were also affected by the disorder of the $ClO_4^-$ anions, but only O(400) was split on two positions in this case. EADP and SAME instructions of ShelXL97 were used to yield reasonable atomic displacement parameters and geometries.

The same disorder model was tried for the isostructural complex [Eu(1bttpam)]$(ClO_4)_3 \cdot 3.65H_2O$; however, the positions of the 3-fold split perchlorate anion were slightly different, and one split position collided with the water molecule containing O(300). A lower occupation factor was therefore assigned for O(300), namely, the sum of the remaining two occupation factors of the aforementioned anion, yielding reasonable hydrogen bonded distances to neighboring acceptor atoms.

Though several crystals from different samples were tested on the diffractometer, the crystal quality, and hence the quality of the diffraction data of [Eu(ttham)]$(ClO_4)_3 \cdot 3H_2O$ was low. The compound crystallizes in the chiral space group $P2_12_12_1$ with four crystallographically independent molecules in the unit cell. Five out of 12 perchlorate anions containing Cl(3) to Cl(7) were split on 2 positions and one out of twelve water molecules was split on 3 positions; their hydrogen atoms could not be localized because of disorder. ISOR and SIMU restraints of ShelXL97 were used to obtain reasonable displacement parameters. Bond distances and angles of the perchlorate anions were restrained using the SAME instruction. Crystallographic data of the compounds are summarized in Table 1.

**NMR and CEST NMR Spectroscopy in Aqueous Solution.** Samples were prepared by dissolving the appropriate amount of complex (20 mM) in aqueous MOPS buffer solution (10 or

(24) Sheldrick, G. M. *SADABS, Bruker−Siemens Area Detector Absorption and Other Correction, 2006/01*; University of Göttingen: Germany, 2006.
(25) *ShelXTL*, 6.14; Bruker AXS Inc.: Madison, WI, 2003.
(26) Sheldrick, G. M.; *ShelXL97*; University of Göttingen: Göttingen, Germany, 1997.

**Table 1.** Crystallographic Data for [Eu(ttham)]$(ClO_4)_3 \cdot 3H_2O$, [Eu(1bttpam)]$(ClO_4)_3 \cdot 3.65H_2O$, and [Tm(1bttpam)]$(ClO_4)_3 \cdot 4H_2O$

| | [Eu(ttham)] $(ClO_4)_3 \cdot 3H_2O$ | [Eu(1bttpam)] $(ClO_4)_3 \cdot 3.65H_2O$ | [Tm(1bttpam)] $(ClO_4)_3 \cdot 4H_2O$ |
|---|---|---|---|
| chem. Formula | $C_{18}H_{42}Cl_3EuN_{10}O_{21}$ | $C_{23}H_{46.3}Cl_3EuN_9O_{20.65}$ | $C_{23}H_{47}Cl_3N_9O_{21}Tm$ |
| Fw | 992.93 | 1037.90 | 1060.98 |
| space group | $P2_12_12_1$, No. 19 | $P2_1/c$, No. 14 | $P2_1/c$, No. 14 |
| $a$, Å | 13.2178(4) | 16.0701(6) | 15.8565(5) |
| $b$, Å | 23.9498(8) | 18.7910(6) | 18.8304(6) |
| $c$, Å | 45.210(2) | 13.0930(4) | 13.0221(4) |
| $\beta$, deg | 90 | 98.482(3) | 98.456(2) |
| $V$, Å | 14311.8(9) | 3910.5(2) | 3845.9(2) |
| $Z$ | 16 | 4 | 4 |
| $T$, K | 100(2) | 100(2) | 100(2) |
| $\rho$ calcd, g·cm$^{-3}$ | 1.843 | 1.763 | 1.832 |
| refl. collected/$2\Theta_{max}$ | 92795/50.00 | 77466/65.00 | 441190/70.00 |
| unique refl./$I > 2\sigma(I)$ | 23894/18498 | 14310/12014 | 16916/15348 |
| no. of params/restr. | 2118/4295 | 568/151 | 581/47 |
| $\lambda$, Å /$\mu$(K$\alpha$), cm$^{-1}$ | 0.71073/20.73 | 0.71073/19.00 | 0.71073/26.09 |
| R1[a]/goodness of fit[b] | 0.0656/1.054 | 0.0611/1.120 | 0.0244/1.113 |
| wR2[c]($I > 2\sigma(I)$) | 0.1343 | 0.1284 | 0.0551 |
| residual density, e Å$^{-3}$ | +1.43/−0.80 | +6.53/−3.32 | +1.72/−1.40 |

[a]) Observation criterion: $I > 2\sigma(I)$. R1 = $\sum||F_o| - |F_c||/\sum|F_o|$. [b]) GooF = $[\sum[w(F_o^2 - F_c^2)^2]/(n-p)]^{1/2}$. [c]) $w$R2 = $[\sum w(F_o^2 - F_c^2)^2/\sum w(F_o^2)^2]^{1/2}$ where $w = 1/\sigma^2(F_o^2) + (aP)^2 + bP$, $P = (F_o^2 + 2F_c^2)/3$.

20 mM). If required, the pH value of the solutions was adjusted by adding small aliquots of either 0.1 M NaOH or 0.1 M HCl stock solutions. To enable frequency locking, a coaxial glass capillary insert filled with deuterated tetrachloroethane was used. NMR spectra were recorded on a Bruker Avance NMR spectrometer equipped with an Oxford wide-bore 7 T superconducting magnet. Regular 1D $^1$H NMR spectra (200 kHz spectral width, 256 k complex data points, 2 $\mu$s excitation pulse, 256 averages) were measured with continuous-wave RF irradiation (duration $t_{sat}$ = 2 s; RF amplitude $B_1$ = 10 $\mu$T) at the $H_2O$ resonance frequency for water suppression. Prior to Fourier transform, the data were apodized with an exponential filter (5 Hz line broadening). All spectra were calibrated relative to the $H_2O$ frequency. CEST spectra were recorded using standard continuous-wave irradiation (2 s pulse duration; 25 $\mu$T RF amplitude) at variable frequencies for selective presaturation of the exchangeable-proton resonances. Typically 511 individual 1D $^1$H NMR spectra were acquired at different values of the presaturation offset frequency (500 Hz intervals up to 127.5 kHz) centered around the water resonance frequency and stored in a single 2D NMR data set. To reconstruct the CEST spectrum, the water signal of each individual spectrum in the 2D data set was integrated and plotted as a function of the saturation frequency offset. From the resulting spectrum the CEST effect was determined using eq 1.

**Syntheses.** Diethyl 2-bromoethylamine-*N*,*N*-diacetate (**5**) was synthesized according to a published procedure.[27] The syntheses of triethylenetetramine-*N*,*N*,*N*′,*N*″,*N*‴,*N*‴′-hexaacetamide (ttham), *N*-benzyl-triethylenetetramine-*N*,*N*′,*N*″,*N*‴,*N*‴′-pentaacetamide (1bttpam), and *N*′-benzyl-triethylenetetramine-*N*,*N*,*N*″,*N*‴,*N*‴′-pentaacetamide (4bttpam) had been described in a previous publication.[23]

**Di-*tert*-butyl *N*,*N*′-Dibenzyl-ethylenediamine-*N*,*N*′-diacetate (3).** A solution of *N*,*N*′-dibenzylethylenediamine (**1**) (15.1 mL, 64.0 mmol) in DMF (40 mL) was added dropwise to a mixture of *tert*-butyl bromoacetate (**2**) (18.9 mL, 128 mmol) and potassium bicarbonate (18.0 g, 180 mmol) in DMF (80 mL), which was cooled in an ice−water bath. The reaction mixture was stirred for 1 h in the ice−water bath and for 20 h at room temperature (RT). Water (240 mL) was added, and the resulting mixture was extracted with toluene (2 × 120 mL). The combined organic layers were subsequently extracted with water (120 mL) and brine (50 mL), dried with magnesium sulfate, and the volatiles were removed by rotary evaporation. A white solid (18.5 g, 65%) was obtained after crystallization from methanol. mp 68 °C. $^1$H NMR ($CDCl_3$, $\delta$/ppm): 7.28 (m, 10H), 3.77 (s, 4H), 3.25 (s, 4H), 2.80 (s, 4H), 1.44 (s, 18H).

**Di-*tert*-butyl Ethylenediamine-*N*,*N*′-diacetate (4).** A mixture of **3** (10.0 g, 43 mmol), 10% palladium hydroxide on carbon powder (1.0 g), and ethanol (250 mL) was hydrogenated (1 bar, RT, 3 h). Filtration over Celite and evaporation of the volatiles yielded pure **4** (5.0 g, 82%). $^1$H NMR ($CDCl_3$, $\delta$/ppm): 3.31 (s, 4H), 2.72 (s, 4H), 1.82 (s, 2H), 1.47 (s, 18H).

**Di-*tert*-butyl *N*,*N*,*N*‴,*N*‴′-Tetra(ethoxy-2-oxoethyl)-triethylenetetramine-*N*′,*N*″-diacetate (6).** A mixture of **4** (5.60 g, 19.4 mmol), diethyl (2-bromoethyl)amine-*N*,*N*-diacetate (**5**) (12.6 g, 42.6 mmol), potassium bicarbonate (6.00 g, 60.0 mmol), and DMF (100 mL) was stirred at 60 °C for 16 h. After cooling to RT, toluene (100 mL) and water (200 mL) were added. The organic layer was separated, and the aqueous layer was extracted with toluene (100 mL). The combined organic layers were subsequently extracted with water (100 mL) and brine (50 mL), dried over magnesium sulfate, and evaporated. Column chromatography (silica−diethyl ether/hexane/triethylamine (75:24:1)) yielded pure **6** as a yellow oil (9.43 g, 68%). $^1$H NMR ($CDCl_3$, $\delta$/ppm): 4.09 (q, $J$ = 7.1 Hz, 8H), 3.51 (s, 8H), 3.25 (s, 4H), 2.74 (m, 8H), 2.65 (s, 4H), 1.38 (s, 18H), 1.19 (t, $J$ = 7.1 Hz, 12H).

**Di-*tert*-butyl *N*,*N*,*N*‴,*N*‴′-Tetra(carbamoylmethyl)-triethylenetetramine-*N*′,*N*″-diacetate ($Bu_2$ttha-tm).** A solution of **6** (1.94 g, 2.70 mmol) in a solution of ammonia in methanol (7 N, 60 mL) was stirred for 4 d at 40 °C. Evaporation and drying over silica yielded pure $Bu_2$ttha-tm (1.63 g, 100%). mp 143−149 °C (decomp.). FT-IR (ATR, cm$^{-1}$): 2459, 2440, 3279 (br), 3125 (br), 2971 (br), 2847, 2836, 1728 (C═O), 1688 (C═O), 1671 (C═O), 1591 (br), 1388, 1365, 1288, 1257, 1224, 1154, 1094, 952, 866, 829, 752, 572, 471. MS (MALDI-TOF, $m/z$): Calcd for $C_{26}H_{51}N_8O_8^+$ ($[M+H]^+$): 603.38, Found: 603.27. $^1$H NMR (DMSO-$d_6$, $\delta$/ppm): 7.58 (s, 4H), 7.10 (s, 4H), 3.24 (s, 4H), 3.03 (s, 8H), 2.65 (t, $J$ = 6.1 Hz, 4H), 2.59 (s, 4H), 2.52 (t, $J$ = 6.1 Hz, 4H), 1.41 (s, 18H). $^{13}$C NMR (DMSO-$d_6$, $\delta$/ppm): 173.2, 170.8, 80.6, 59.1, 56.1, 53.5, 52.6, 52.4, 28.2.

***N*,*N*,*N*‴,*N*‴′-Tetra(ethoxy-2-oxoethyl)-triethylenetetramine-*N*′,*N*″-diacetic acid (7).** A solution of **6** (4.90 g, 6.82 mmol) in dichloromethane-trifluoroacetic acid (1:1, 300 mL) was stirred at RT for 5 h. After evaporation, the mixture was co-evaporated with dichloromethane (2 × 150 mL) and kept under vacuum overnight. A yellow viscous material (10.7 g) was obtained that contained considerable amounts of dichloromethane and trifluoroacetic acid. This material was used without further purification in the next step.

(27) Williams, M. A.; Rapoport, H. *J. Org. Chem.* **1993**, *58*, 1151–1158.

***N,N,N′′,N′′′*-Tetra(carbamoylmethyl)-triethylenetetramine-*N′,N′′*-diacetic acid ($H_2$ttha-tm).** A solution of raw **7** (as obtained in the previous step) in a solution of ammonia in methanol (7 N, 250 mL) was stirred for 5 d at RT. Pure $H_2$ttha-tm precipitated as a colorless crystalline solid. (1.70 g, 51% over two steps). mp > 140 °C (decomp.). FT-IR (ATR, $cm^{-1}$): 3410 (br), 3333 (br), 3194 (br), 2821, 1673 (C=O), 1647 (C=O), 1382, 1332, 1286, 1102, 967, 831, 788, 690. MS (MALDI-TOF, *m*/*z*): Calcd for $C_{18}H_{35}N_8O_8^+$ ($[M+H]^+$): 491.26, Found: 491.15. $^1$H NMR (DMSO-$d_6$, $\delta$/ppm): 7.74 (s, 4H), 7.12 (s, 4H), 3.27 (s, 4H), 3.09 (s, 8H), 2.97 (s, 4H), 2.97 (m, 4H), 2.69 (t, $J$ = 5.6 Hz, 4H), (acidic H observed as very broad signal around 6 ppm). $^{13}$C NMR (DMSO-$d_6$, $\delta$/ppm): 173.3, 171.6, 56.1, 52.2, 51.8, 51.7.

**[Ln(ttham)]$Cl_3$ (L = ttham). General Procedure.** To a suspension of ttham (0.50 g, 1.0 mmol) in methanol (30 mL) was added $LnCl_3 \cdot xH_2O$ (1.0 mmol). The suspension was heated under reflux for 0.5 h, whereupon a clear solution was obtained (within a few minutes). After cooling to RT, propionitrile (50 mL) was added, and the solution was filtered into a covered crystallization dish. Overnight a crystalline precipitate was formed, which was collected by filtration, washed with acetone, and dried. The solid was recrystallized from methanol/propionitrile (1:2, 60 mL) to obtain a crystalline product, which was dried and stored over silica.

**[La(ttham)]$Cl_3$.** Colorless microcrystals. Yield: 66%. Anal. (%) Calcd for $C_{18}H_{36}N_{10}O_6La_1Cl_3 \cdot 3H_2O$: C, 27.4; H, 5.4; N, 17.8; La, 17.6; Cl, 13.5. Found: C, 27.1; H, 5.3; N, 16.6; La, 18.2; Cl, 13.5. FT-IR (ATR, $cm^{-1}$): 3262 (br), 3112 (br), 1680 (C=O), 1662 (C=O), 1598 (C=O), 1451, 1326, 1117, 654, 438. MS (MALDI-TOF, *m*/*z*): Found (Calcd) 625.12 (625.17, $[La(H_{-2}L)]^+$). MS (ESI, *m*/*z*): Found (Calcd) 696.8 (697.1, $[La(L)Cl_2]^+$); 660.9 (661.2, $[La(H_{-1}L)Cl]^+$); 625.2 (625.2, $[La(H_{-2}L)]^+$); 331.1 (331.1, $[La(L)Cl]^{2+}$); 313.2 (313.1, $[La(H_{-1}L)]^{2+}$); 209.3 (209.1, $[La(L)]^{3+}$).

**[Ce(ttham)]$Cl_3$.** Colorless microcrystals. Yield: 64%. Anal. (%) Calcd for $C_{18}H_{36}N_{10}O_6Ce_1Cl_3 \cdot 3H_2O$: C, 27.4; H, 5.4; N, 17.8; Ce, 17.8; Cl, 13.5. Found: C, 25.6; H, 5.9; N, 14.8; Ce, 20.7; Cl, 12.8. FT-IR (ATR, $cm^{-1}$): 3266 (br), 3117 (br), 1680 (C=O), 1661 (C=O), 1598, (C=O), 1450, 1326, 1117, 653, 440. MS (MALDI-TOF, *m*/*z*): Found (Calcd) 626.09 (626.17, $[Ce(H_{-2}L)]^+$). MS (ESI, *m*/*z*): Found (Calcd) 697.9 (698.1, $[Ce(L)Cl_2]^+$); 661.9 (662.2, $[Ce(H_{-1}L)Cl]^+$); 626.2 (626.2, $[Ce(H_{-2}L)]^+$); 331.6 (331.6, $[Ce(L)Cl]^{2+}$); 313.7 (313.6, $[Ce(H_{-1}L)]^{2+}$); 209.6 (209.4, $[Ce(L)]^{3+}$).

**[Pr(ttham)]$Cl_3$.** Light green microcrystals. Yield: 61%. Anal. (%) Calcd for $C_{18}H_{36}N_{10}O_6Pr_1Cl_3 \cdot 3H_2O$: C, 27.4; H, 5.4; N, 17.7; Pr, 17.8; Cl, 13.5. Found: C, 27.6; H, 6.0; N, 17.4; Pr, 16.1; Cl, 12.2. FT-IR (ATR, $cm^{-1}$): 3274 (br), 3121 (br), 1660 (C=O), 1600 (C=O), 1456, 1328, 1121, 653, 444. MS (MALDI-TOF, *m*/*z*): Found (Calcd) 627.39 (627.17, $[Pr(H_{-2}L)]^+$). MS (ESI, *m*/*z*): Found (Calcd) 698.8 (699.1, $[Pr(L)Cl_2]^+$); 662.9 (663.2, $[Pr(H_{-1}L)Cl]^+$); 627.2 (627.2, $[Pr(H_{-2}L)]^+$); 332.1 (332.1, $[Pr(L)Cl]^{2+}$); 314.1 (314.1, $[Pr(H_{-1}L)]^{2+}$); 209.9 (209.7, $[Pr(L)]^{3+}$).

**[Nd(ttham)]$Cl_3$.** Light purple microcrystals. Yield: 71%. Anal. (%) Calcd for $C_{18}H_{36}N_{10}O_6Nd_1Cl_3 \cdot 3H_2O$: C, 27.3; H, 5.3; N, 17.7; Nd, 18.2; Cl, 13.4. Found: C, 29.1; H, 5.5; N, 17.6; Nd, 18.1; Cl, 12.9. FT-IR (ATR, $cm^{-1}$): 3266 (br), 3118 (br), 1660 (C=O), 1599 (C=O), 1450, 1326, 1118, 654, 443. MS (MALDI-TOF, *m*/*z*): Found (Calcd) 628.11 (628.17, $[Nd(H_{-2}L)]^+$). MS (ESI, *m*/*z*): Found (Calcd) 699.8 (700.1, $[Nd(L)Cl_2]^+$); 663.9 (664.2, $[Nd(H_{-1}L)Cl]^+$); 628.3 (628.2, $[Nd(H_{-2}L)]^+$); 332.6 (332.6, $[Nd(L)Cl]^{2+}$); 314.7 (314.6, $[Nd(H_{-1}L)]^{2+}$); 209.4 (210.3, $[Nd(L)]^{3+}$).

**[Sm(ttham)]$Cl_3$.** Off-white microcrystals. Yield: 70%. Anal. (%) Calcd for $C_{18}H_{36}N_{10}O_6Sm_1Cl_3 \cdot 3H_2O$: C, 27.1; H, 5.3; N, 17.5; Sm, 18.8; Cl, 13.3. Found: C, 29.0; H, 5.5; N, 17.5; Sm, 17.8; Cl, 12.5. FT-IR (ATR, $cm^{-1}$): 3272 (br), 3124 (br), 1658 (C=O), 1598 (C=O), 1327, 1123, 655, 447. MS (MALDI-TOF, *m*/*z*): Found (Calcd) 638.17 (638.19, $[Sm(H_{-2}L)]^+$). MS (ESI, *m*/*z*): Found (Calcd) 709.8 (710.1, $[Sm(L)Cl_2]^+$); 674.0 (674.2, $[Sm(H_{-1}L)Cl]^+$); 638.2 (638.2, $[Sm(H_{-2}L)]^+$); 337.6 (337.6, $[Sm(L)Cl]^{2+}$); 319.7 (319.6, $[Sm(H_{-1}L)]^{2+}$); 213.6 (213.4, $[Sm(L)]^{3+}$).

**[Eu(ttham)]$Cl_3$.** Colorless needles. Yield: 78%. Anal. (%) Calcd for $C_{18}H_{36}N_{10}O_6Eu_1Cl_3 \cdot 3H_2O$: C, 27.0; H, 5.3; N, 17.5; Eu, 19.0; Cl, 13.3. Found: C, 27.6; H, 5.4; N, 17.3; Eu, 17.8; Cl, 14.3. FT-IR (ATR, $cm^{-1}$): 3275 (br), 3121 (br), 1683 (C=O), 1659 (C=O), 1600 (C=O), 1451, 1326, 1120, 655, 444. MS (MALDI-TOF, *m*/*z*): Found (Calcd) 639.07 (639.19, $[Eu(H_{-2}L)]^+$). MS (ESI, *m*/*z*): Found (Calcd) 710.8 (711.1, $[Eu(L)Cl_2]^+$); 674.9 (675.2, $[Eu(H_{-1}L)Cl]^+$); 639.1 (639.2, $[Eu(H_{-2}L)]^+$); 338.1 (338.1, $[Eu(L)Cl]^{2+}$); 320.2 (320.1, $[Eu(H_{-1}L)]^{2+}$); 213.9 (213.7, $[Eu(L)]^{3+}$).

**[Gd(ttham)]$Cl_3$.** Colorless microcrystals. Yield: 76%. Anal. (%) Calcd for $C_{18}H_{36}N_{10}O_6Gd_1Cl_3 \cdot 3H_2O$: C, 26.8; H, 5.3; N, 17.4; Gd, 19.5; Cl, 13.2. Found: C, 28.0; H, 5.5; N, 17.4; Gd, 20.4; Cl, 13.2. FT-IR (ATR, $cm^{-1}$): 3271 (br), 3120 (br), 1682 (C=O), 1659 (C=O), 1600 (C=O), 1452, 1325, 1120, 655, 446. MS (MALDI-TOF, *m*/*z*): Found (Calcd) 644.06 (644.19, $[Gd(H_{-2}L)]^+$). MS (ESI, *m*/*z*): Found (Calcd) 715.9 (716.1, $[Gd(L)Cl_2]^+$); 679.9 (680.2, $[Gd(H_{-1}L)Cl]^+$); 644.1 (644.2, $[Gd(H_{-2}L)]^+$); 340.6 (340.6, $[Gd(L)Cl]^{2+}$); 322.7 (322.6, $[Gd(H_{-1}L)]^{2+}$); 214.6 (214.7, $[Gd(L)]^{3+}$).

**[Tb(ttham)]$Cl_3$.** Colorless microcrystals. Yield: 63%. Anal. (%) Calcd for $C_{18}H_{36}N_{10}O_6Tb_1Cl_3 \cdot 3H_2O$: C, 26.8; H, 5.2; N, 17.3; Tb, 19.7; Cl, 13.2. Found: C, 28.0; H, 5.3; N, 17.1; Tb, 19.7; Cl, 12.3. FT-IR (ATR, $cm^{-1}$): 3278 (br), 3123 (br), 1684 (C=O), 1659 (C=O), 1600 (C=O), 1451, 1326, 1120, 657, 449. MS (MALDI-TOF, *m*/*z*): Found (Calcd) 645.19 (645.12, $[Tb(H_{-2}L)]^+$). MS (ESI, *m*/*z*): Found (Calcd) 716.8 (717.5, $[Tb(L)Cl_2]^+$); 680.9 (681.2, $[Tb(H_{-1}L)Cl]^+$); 645.2 (645.2, $[Tb(H_{-2}L)]^+$); 341.1 (341.1, $[Tb(L)Cl]^{2+}$); 323.1 (323.1, $[Tb(H_{-1}L)]^{2+}$); 216.0 (215.7, $[Tb(L)]^{3+}$).

**[Dy(ttham)]$Cl_3$.** Colorless microcrystals. Yield: 60%. Anal. (%) Calcd for $C_{18}H_{36}N_{10}O_6Dy_1Cl_3 \cdot 3H_2O$: C, 26.6; H, 5.2; N, 17.3; Dy, 20.0; Cl, 13.1. Found: C, 27.6; H, 5.2; N, 17.1; Ho, 20.3; Cl, 12.4. FT-IR (ATR, $cm^{-1}$): 3277 (br), 3121 (br), 1685 (C=O), 1659 (C=O), 1601 (C=O), 1452, 1326, 1120, 656, 449. MS (MALDI-TOF, *m*/*z*): Found (Calcd) 650.09 (650.20, $[Dy(H_{-2}L)]^+$). MS (ESI, *m*/*z*): Found (Calcd) 721.8 (722.2, $[Dy(L)Cl_2]^+$); 685.9 (686.2, $[Dy(H_{-1}L)Cl]^+$); 650.2 (650.2, $[Dy(H_{-2}L)]^+$); 343.6 (343.6, $[Dy(L)Cl]^{2+}$); 325.7 (325.6, $[Dy(H_{-1}L)]^{2+}$); 216.8 (216.7, $[Dy(L)]^{3+}$).

**[Ho(ttham)]$Cl_3$.** Off-white microcrystals. Yield: 64%. Anal. (%) Calcd for $C_{18}H_{36}N_{10}O_6Ho_1Cl_3 \cdot 3H_2O$: C, 26.6; H, 5.2; N, 17.2; Ho, 20.3; Cl, 13.1. Found: C, 27.8; H, 5.4; N, 17.4; Ho, 20.7; Cl, 12.6. FT-IR (ATR, $cm^{-1}$): 3278 (br), 3121 (br), 1682 (C=O), 1659 (C=O), 1600 (C=O), 1453, 1325, 1121, 655, 449. MS (MALDI-TOF, *m*/*z*): Found (Calcd) 651.20 (651.20, $[Ho(H_{-2}L)]^+$). MS (ESI, *m*/*z*): Found (Calcd) 723.2 (722.7, $[Ho(L)Cl_2]^+$); 686.9 (687.2, $[Ho(H_{-1}L)Cl]^+$); 651.2 (651.2, $[Ho(H_{-2}L)]^+$); 344.1 (344.1, $[Ho(L)Cl]^{2+}$); 326.2 (326.1, $[Ho(H_{-1}L)]^{2+}$); 217.3 (217.1, $[Ho(L)]^{3+}$).

**[Er(ttham)]$Cl_3$.** Light pink microcrystals. Yield: 69%. Anal. (%) Calcd for $C_{18}H_{36}N_{10}O_6Er_1Cl_3 \cdot 3H_2O$: C, 26.5; H, 5.2; N, 17.2; Er, 20.5; Cl, 13.0. Found: C, 28.2; H, 5.3; N, 17.5; Er, 21.4; Cl, 12.5. FT-IR (ATR, $cm^{-1}$): 3282 (br), 3122 (br), 1684 (C=O), 1658 (C=O), 1601 (C=O), 1453, 1325, 1121, 655, 450. MS (MALDI-TOF, *m*/*z*): Found (Calcd) 652.12 (652.20, $[Er(H_{-2}L)]^+$). MS (ESI, *m*/*z*): Found (Calcd) 652.2 (655.2, $[Er(H_{-2}L)]^+$); 344.5 (344.6, $[Er(L)Cl]^{2+}$); 326.7 (326.6, $[Er(H_{-1}L)]^{2+}$); 218.3 (218.1, $[Er(L)]^{3+}$).

**[Tm(ttham)]$Cl_3$.** Colorless microcrystals. Yield: 55%. Anal. (%) Calcd for $C_{18}H_{36}N_{10}O_6Tm_1Cl_3 \cdot 3H_2O$: C, 26.4; H, 5.2; N, 17.1; Tm, 20.7; Cl, 13.0. Found: C, 26.9; H, 5.3; N, 16.9; Tm, 20.7; Cl, 12.6. FT-IR (ATR, $cm^{-1}$): 3240 (br), 3149 (br), 1675 (C=O), 1648 (C=O), 1604 (C=O), 1461, 1322, 1118, 658, 455. MS (MALDI-TOF, *m*/*z*): Found (Calcd) 655.19 (655.20, $[Tm(H_{-2}L)]^+$). MS (ESI, *m*/*z*): Found (Calcd) 726.7 (727.2,

$[Tm(L)Cl_2]^+$); 690.9 (691.2, $[Tm(H_{-1}L)Cl]^+$); 655.2 (655.2, $[Tm(H_{-2}L)]^+$); 346.1 (346.1, $[Tm(L)Cl]^{2+}$); 328.1 (328.1, $[Tm(H_{-1}L)]^{2+}$); 219.3 (219.1, $[Tm(L)]^{3+}$).

**[Yb(ttham)]Cl$_3$.** Colorless needles as reported previously.[23]

**[Lu(ttham)]Cl$_3$.** Colorless microcrystals. Yield: 58%. Anal. (%) Calcd for $C_{18}H_{36}N_{10}O_6Lu_1Cl_3 \cdot 3H_2O$: C, 26.2; H, 5.1; N, 17.0; Lu, 21.2; Cl, 12.9. Found: C, 27.8; H, 5.8; N, 17.5; Lu, 21.1; Cl, 12.9. FT-IR (ATR, cm$^{-1}$): 3251 (br), 3165 (br), 1676 (C=O), 1651 (C=O), 1607 (C=O), 1431, 1323, 659, 456. MS (MALDI-TOF, *m*/*z*): Found (Calcd) 661.18 (661.21, $[Lu(H_{-2}L)]^+$). MS (ESI, *m*/*z*): Found (Calcd) 732.9 (733.2, $[Lu(L)Cl_2]^+$); 696.9 (697.2, $[Lu(H_{-1}L)Cl]^+$); 661.2 (661.2, $[Lu(H_{-2}L)]^+$); 349.1 (349.1, $[Lu(L)Cl]^{2+}$); 331.3 (331.1, $[Lu(H_{-1}L)]^{2+}$); 221.3 (221.1, $[Lu(L)]^{3+}$).

**[Ln(1bttpam)]Cl$_3$ (L = 1bttpam). General Procedure.** To a suspension of 1bttpam (0.30 g, 0.58 mmol) in methanol (20 mL) was added $LnCl_3 \cdot xH_2O$ (0.58 mmol). The suspension was heated under reflux for 0.5 h, whereupon a clear solution was obtained (within a few minutes). At RT, propionitrile (30 mL) was added, and the solution was filtered into a covered crystallization dish. Within a few days a crystalline precipitate was formed, which was collected by filtration, washed with acetone, and dried. The solid was recrystallized from methanol/propionitrile (1:2, 45 mL) to obtain a crystalline product, which was dried and stored over silica.

**[Eu(1bttpam)]Cl$_3$.** Colorless crystals. Yield: 79%. Anal. (%) Calcd for $C_{23}H_{39}N_9O_5Eu_1Cl_3 \cdot 4H_2O$: C, 32.4; H, 5.6; N, 14.8; Eu, 17.8; Cl, 12.5. Found: C, 31.7; H, 5.3; N, 14.3; Eu, 17.8; Cl, 12.1. FT-IR (ATR, cm$^{-1}$): 3330 (br), 3148 (br), 2800, 1655 (C=O), 1598 (C=O), 1584 (C=O), 1454, 1426, 1091, 1083, 1054, 911, 749, 705, 647. MS (MALDI-TOF, *m*/*z*): Found (Calcd) 672.0 (672.2, $[Eu(H_{-2}L)]^+$). MS (HR-ESI, *m*/*z*): Found (Calcd) 672.238 (672.213, $[Eu(H_{-2}L)]^+$).

**[Tm(1bttpam)]Cl$_3$.** Stacked, colorless crystal plates. Yield: 56%. Anal. (%) Calcd for $C_{23}H_{39}N_9O_5Tm_1Cl_3 \cdot 3H_2O$: C, 32.5; H, 5.3; N, 14.8; Tm, 19.9; Cl, 12.5. Found: C, 32.1; H, 5.3; N, 14.6; Tm, 19.9; Cl, 11.8. FT-IR (ATR, cm$^{-1}$): 3307 (br), 3102 (br), 2800, 1663 (C=O), 1594 (C=O), 1450, 1419, 1092, 1084, 1054, 918, 749, 709, 648. MS (MALDI-TOF, *m*/*z*): Found (Calcd) 688.1 (688.2, $[Tm(H_{-2}L)]^+$). MS (HR-ESI, *m*/*z*): Found (Calcd) 688.278 (688.226, $[Tm(H_{-2}L)]^+$).

**[Ln(4bttpam)]Cl$_3$ (L = 4bttpam). General Procedure.** To a suspension of 4bttpam (0.50 g, 0.96 mmol) in methanol (30 mL) was added $LnCl_3 \cdot xH_2O$ (0.96 mmol). The suspension was heated under reflux for 0.5 h, whereupon a clear solution was obtained (within a few minutes). At RT, ethyl acetate (60 mL) was added, and the solution was filtered into a covered crystallization dish. Within a few days a crystalline precipitate was formed, which was collected by filtration, washed with acetone, and dried. The solid was recrystallized from methanol/ethyl acetate (1:2, 60 mL) to obtain a crystalline product, which was dried and stored over silica.

**[Eu(4bttpam)]Cl$_3$.** Large, colorless crystal plates. Yield: 63%. Anal. (%) Calcd for $C_{23}H_{39}N_9O_5Eu_1Cl_3 \cdot 5H_2O$: C, 31.8; H, 5.7; N, 14.5; Eu, 17.5; Cl, 12.2. Found: C, 30.5; H, 5.7; N, 13.8; Eu, 17.8; Cl, 11.6. FT-IR (ATR, cm$^{-1}$): 3264 (br), 3097 (br), 1659 (C=O), 1598 (C=O), 1453, 1429, 1324, 1095, 703. MS (HR-ESI, *m*/*z*): Found (Calcd) 672.233 (672.213, $[Eu(H_{-2}L)]^+$); 708.203 (708.190, $[Eu(H_{-1}L)Cl]^+$).

**[Tm(4bttpam)]Cl$_3$.** Light yellow microcrystals. Yield: 51%. Anal. (%) Calcd for $C_{23}H_{39}N_9O_5Tm_1Cl_3 \cdot 4H_2O$: C, 31.8; H, 5.5; N, 14.5; Tm, 19.4; Cl, 12.2. Found: C, 31.9; H, 5.4; N, 14.5; Tm, 20.5; Cl, 11.8. FT-IR (ATR, cm$^{-1}$): 3273 (br), 3075 (br), 1660 (C=O), 1598 (C=O), 1453, 1428, 1320, 1096, 703. MS (HR-ESI, *m*/*z*): Found (Calcd) 688.270 (688.226, $[Tm(H_{-2}L)]^+$); 724.217 (724.203, $[Tm(H_{-1}L)Cl]^+$).

**[Ln(Bu$_2$ttha-tm)]Cl$_3$ (L = Bu$_2$ttha-tm). General Procedure.** To a suspension of Bu$_2$ttha-tm (0.60 g, 1.0 mmol) in methanol (30 mL) was added $LnCl_3 \cdot xH_2O$ (1.0 mmol). The suspension was stirred at 35 °C for 3 h, whereupon a clear solution was obtained (within 0.5 h). At RT, propionitrile (60 mL) was added, and the solution was filtered into a covered crystallization dish. Within a few days a fine crystalline precipitate was formed, which was collected by filtration, washed with acetone, and dried. The solid was recrystallized from methanol/ethylacetate (1:2, 60 mL) to obtain a microcrystalline product, which was dried and stored over silica.

**[Eu(Bu$_2$ttha-tm)]Cl$_3$.** Light yellow microcrystals. Yield: 67%. Anal. (%) Calcd for $C_{26}H_{50}N_8O_8Eu_1Cl_3 \cdot 2H_2O$: C, 34.8; H, 6.1; N, 12.5; Eu, 16.9; Cl, 11.9. Found: C, 33.1; H, 5.7; N, 12.7; Eu, 17.5; Cl, 12.2. FT-IR (ATR, cm$^{-1}$): 3097 (br), 2980, 2930, 2885, 1727, 1672 (C=O), 1619 (C=O), 1584 (C=O), 1454, 1428, 1242, 1159, 1093, 910, 657, 462, 436. MS (HR-ESI, *m*/*z*): Found (Calcd) 753.295 (753.281, $[Eu(H_{-2}L)]^+$); 697.235 (697.281, $[Eu(H_{-1}Bu_{-1}L)]^+$); 641.179 (641.156, $[Eu(Bu_{-2}L)]^+$).

**[Tm(Bu$_2$ttha-tm)]Cl$_3$.** Off-white microcrystals. Yield: 24%. Anal. (%) Calcd for $C_{26}H_{50}N_8O_8Tm_1Cl_3 \cdot 1H_2O$: C, 34.9; H, 5.8; N, 12.5; Tm, 18.9; Cl, 11.9. Found: C, 32.6; H, 5.4; N, 12.6; Tm, 19.5; Cl, 11.5. FT-IR (ATR, cm$^{-1}$): 3090 (br), 2978, 2931, 2897, 1725, 1673 (C=O), 1622 (C=O), 1590 (C=O), 1454, 1428, 1241, 1160, 1093, 916, 659, 466, 441. MS (HR-ESI, *m*/*z*): Found (Calcd) 769.308 (769.294, $[Tm(H_{-2}L)]^+$); 713.255 (713.231, $[Tm(H_{-1}Bu_{-1}L)]^+$); 657.220 (657.169, $[Tm(Bu_{-2}L)]^+$).

**[Ln(ttha-tm)]Cl (L = ttha-tm$^{2-}$). General Procedure.** To a suspension of H$_2$ttha-tm (0.49 g, 1.0 mmol) in methanol (20 mL) was added $LnCl_3 \cdot xH_2O$ (1.0 mmol). The suspension was heated under reflux for 10 min, whereupon a clear solution was obtained. A solution of ammonia in methanol (2.0 mL, 1.0 M) was added and heating was continued for 10 min. At RT, propionitrile (40 mL) was added, and the solution was filtered into a covered crystallization dish. Overnight a crystalline precipitate was formed, which was collected by filtration, washed with acetone, and dried. The solid was recrystallized from methanol/ethylacetate (1:2, 60 mL) to obtain a crystalline product, which was dried and stored over silica.

**[Eu(ttha-tm)]Cl.** Colorless spheres. Yield: 60%. Anal. (%) Calcd for $C_{18}H_{32}N_8O_8Eu_1Cl_1 \cdot 3H_2O$: C, 29.6; H, 5.2; N, 15.4; Eu, 20.8; Cl, 4.9. Found: C, 29.1; H, 5.2; N, 15.1; Eu, 18.8; Cl, 5.1. FT-IR (ATR, cm$^{-1}$): 3265 (br), 3149 (br), 2988, 2876, 1666 (C=O), 1605 (C=O), 1583 (C=O), 1410, 1326, 1271, 1098, 917, 843, 657, 593, 433. MS (MALDI-TOF, *m*/*z*): Found (Calcd) 641.1 (641.2, $[Eu(L)]^+$). MS (HR-ESI, *m*/*z*): Found (Calcd) 641.285 (641.156, $[Eu(L)]^+$).

**[Tm(ttha-tm)]Cl.** Colorless microcrystals. Yield: 63%. Anal. (%) Calcd for $C_{18}H_{32}N_8O_8Tm_1Cl_1 \cdot 2H_2O$: C, 29.7; H, 5.0; N, 15.4; Tm, 23.2; Cl, 4.9. Found: C, 29.6; H, 4.9; N, 15.5; Tm, 23.0; Cl, 4.9. FT-IR (ATR, cm$^{-1}$): 3545 (br), 3286 (br), 3102 (br), 2937, 2864, 1700 (C=O), 1664 (C=O), 1603 (C=O), 1390, 1323, 1283, 1095, 921, 830, 702, 655, 427. MS (MALDI-TOF, *m*/*z*): Found (Calcd) 657.1 (657.2, $[Tm(L)]^+$). MS (HR-ESI, *m*/*z*): Found (Calcd) 657.368 (657.169, $[Tm(L)]^+$).

## Results

**Syntheses.** The tetramides Bu$_2$ttha-tm and H$_2$ttha-tm (Scheme 1) were prepared by reaction of ammonia with the corresponding ethyl esters **6** and **7**, respectively, similar to the earlier described synthesis of ttham, 1bttpam, and 4bttpam (Chart 1).[23] **7** was obtained from **6** after selective deprotection of the *tert*-butyl carboxylate groups with trifluoroacetic acid. An alternative route to H$_2$ttha-tm via deprotection of Bu$_2$ttha-tm yielded an impure product in a lower yield. The mixed ester **6** was synthesized similarly to the precursor of 1bttpam by reaction of 2 equiv of bromide **5** with diamine **4**. The latter compound was relatively stable with respect to cyclization, which is known to yield 1-benzylpiperazin-2-one ring derivatives in the case of more reactive esters, such as ethyl

**Scheme 1.** Synthesis of $Bu_2$ttha-tm and $H_2$ttha-tm

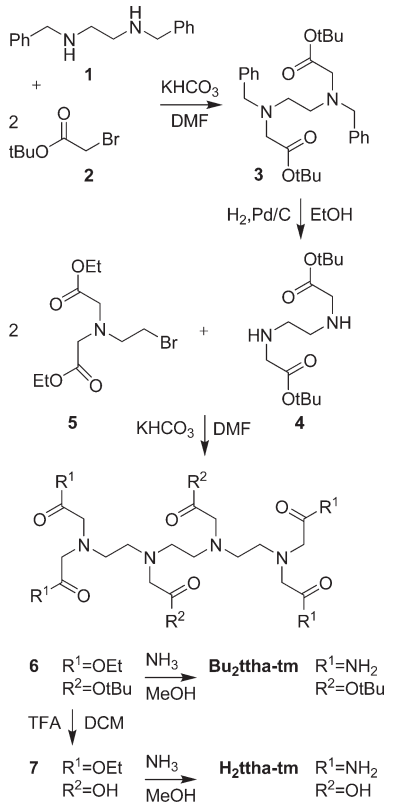


aminoacetates.[23] Diamine **4** was obtained upon alkylation of diamine **1** with 2 equiv of bromide **2**, followed by debenzylation of intermediate **3** by hydrogenation. Alternative synthesis routes to **6** starting from triethylenetetramine derivatives were less successful because of the extensive formation of 1-benzylpiperazin-2-one ring derivatives yielding only impure products and generally low yields.

Lanthanide complexes of the ligands ttham, 1bttpam, 4bttpam, $Bu_2$ttha-tm, and $H_2$ttha-tm were prepared by reaction of stoichiometric amounts of the respective ligands with lanthanide trichlorides in methanol. In the preparation of $H_2$ttha-tm complexes, ammonia in methanol solution was added as balancing base. The mononuclear complexes $[Ln(L)]Cl_3$ (L = ttham, 1bttpam, 4bttpam, $Bu_2$ttha-tm) and [Ln(ttha-tm)]Cl were found to be highly water-soluble and moderately hygroscopic as solids. All complexes could, nevertheless, be recrystallized from methanol/propionitrile or methanol/ethyl acetate. Of the ligand ttham, all lanthanide complexes $[Ln(ttham)]Cl_3$ (Ln = La−Lu, except Pm) were isolated and characterized. To probe the coordination properties of the remaining four ligands, their $Eu^{3+}$ and $Tm^{3+}$ complexes were prepared. The synthesis and characterization of the ytterbium complexes of ttham, 1bttpam, and 4bttpam had been reported earlier.[23] The complexes $[Ln(Bu_2ttha\text{-}tm)]Cl_3$ were found to exhibit a low stability in aqueous solution. NMR studies indicated a quick hydrolysis of the *tert*-butyl ester groups even at RT, presumably facilitated by the coordinated lanthanide trication. The $Bu_2$ttha-tm complexes were therefore not further studied in aqueous solution.

**Crystal Structure Analyses.** X-ray quality crystals were grown of the perchlorate salts of $[Eu(ttham)]^{3+}$, $[Eu(1bttpam)]^{3+}$, and $[Tm(1bttpam)]^{3+}$ upon slow solvent evaporation from aqueous solutions of their respective chloride salts in the presence of excess sodium perchlorate.

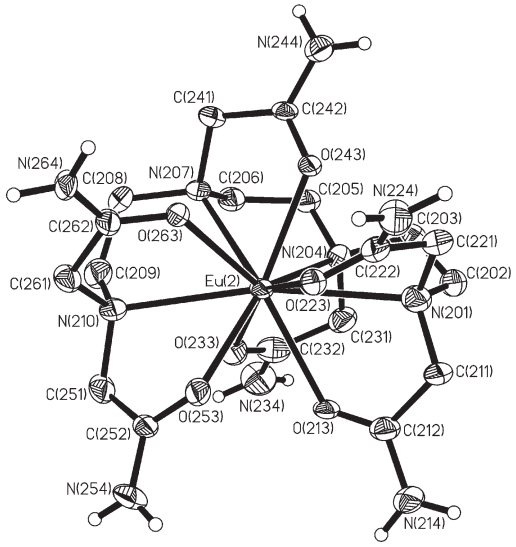


**Figure 1.** ORTEP of the complex cation of $[Eu(ttham)](ClO_4)_3 \cdot 3H_2O$ at a 40% probability level.

The structure of $[Eu(ttham)](ClO_4)_3 \cdot 3H_2O$ consists of the complex, perchlorate anions, and water of hydration. The studied crystal (space group $P2_12_12_1$) contains four independent complex molecules exhibiting only small structural differences. All four molecules are monomeric and consist of the ttham ligand wrapped around the 10-coordinate europium cation (Figure 1). In the first coordination sphere the metal is surrounded by four amine nitrogen and six carboxamide oxygen atoms located at typical distances from the metal (average values: $d$(Eu−O) = 245.3 pm, $d$(Eu−N) = 272.6 pm) and forming a distorted bicapped square antiprism, in which N1 and N10 are the caps, and N4, O13, O23, O43 and N7, O33, O53, O63 constitute the respective bases.

$[Eu(1bttpam)](ClO_4)_3 \cdot 3.65H_2O$ and $[Tm(1bttpam)](ClO_4)_3 \cdot 4H_2O$ both crystallize in the space group $P2_1/c$ comprising crystal water, perchlorate anions, and single independent monomeric complex cations, which are structurally very similar (Figure 2). The first coordination sphere of the 9-coordinate lanthanide cations is composed of four amine nitrogen and five carboxamide oxygen atoms.

Their distorted geometry is best described as a monocapped square antiprism, in which N10, O13, O23, O33, and N1, N4, N7, O43 define the square planes, the latter one being capped by O53. The average twist angles between the two squares are 41.2° for the Eu- and 41.6° for the Tm-compound, which is close to the 45° for an ideal antiprism.

In $[Eu(1bttpam)]^{3+}$ the average europium−oxygen and europium−nitrogen distances ($d$(Eu−O) = 241.3 pm, $d$(Eu−N) = 267.0 pm) show a consistent trend to being shorter by some 4.0 and 5.6 pm, respectively, compared to the 10-coordinate $[Eu(ttham)]^{3+}$. This is indicative for the presence of substantial steric crowding in the 10-coordinate ttham complex, which most likely prevents the occupation of a tenth coordination site by a water molecule in the 9-coordinate $[Eu(1bttpam)]^{3+}$.[28] In [Tm

(28) Cotton, S. A. *C. R. Chimie* **2005**, *8*, 129–145.

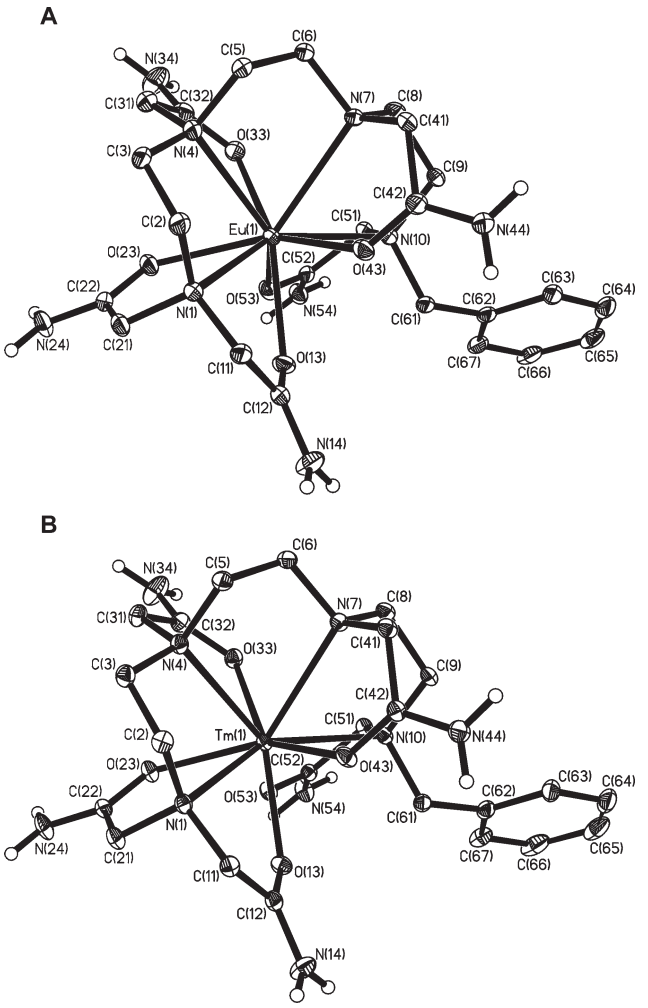


**Figure 2.** Oak Ridge Thermal Ellipsoid Plots (ORTEPs) of the complex cations of [Eu(1bttpam)]$(ClO_4)_3 \cdot 3.65H_2O$ at a 40% probability level (A) and [Tm(1bttpam)]$(ClO_4)_3 \cdot 4H_2O$ at a 50% probability level.

$(1bttpam)]^{3+}$ the average thulium−oxygen and thulium−nitrogen distances ($d$(Tm−O) = 233.3 pm, $d$(Tm−N) = 261.8 pm) are even shorter by some 8.0 and 5.2 pm, respectively, compared to $[Eu(1bttpam)]^{3+}$ illustrating the lanthanide contraction effect.[29,30]

**Infrared and Raman Spectroscopy.** Infrared spectra of solid chloride salts were measured of all ttham complexes ($[Ln(ttham)]^{3+}$, Ln = La−Lu, except Pm) as well as of the $Eu^{3+}$ and $Tm^{3+}$ complexes of 1bttpam, 4bttpam, ttha-$tm^{2-}$, and $Bu_2$ttha-tm to probe structural changes across the lanthanide series. In general, solid state infrared and Raman spectroscopy are very sensitive to conformational and structural changes, in particular, if the latter are accompanied by a change of the coordination number in lanthanide complexes, in which the ligand composition remains unaltered.[31,32]

The IR spectral region dominated by the amide I and II absorption bands of six representative ttham

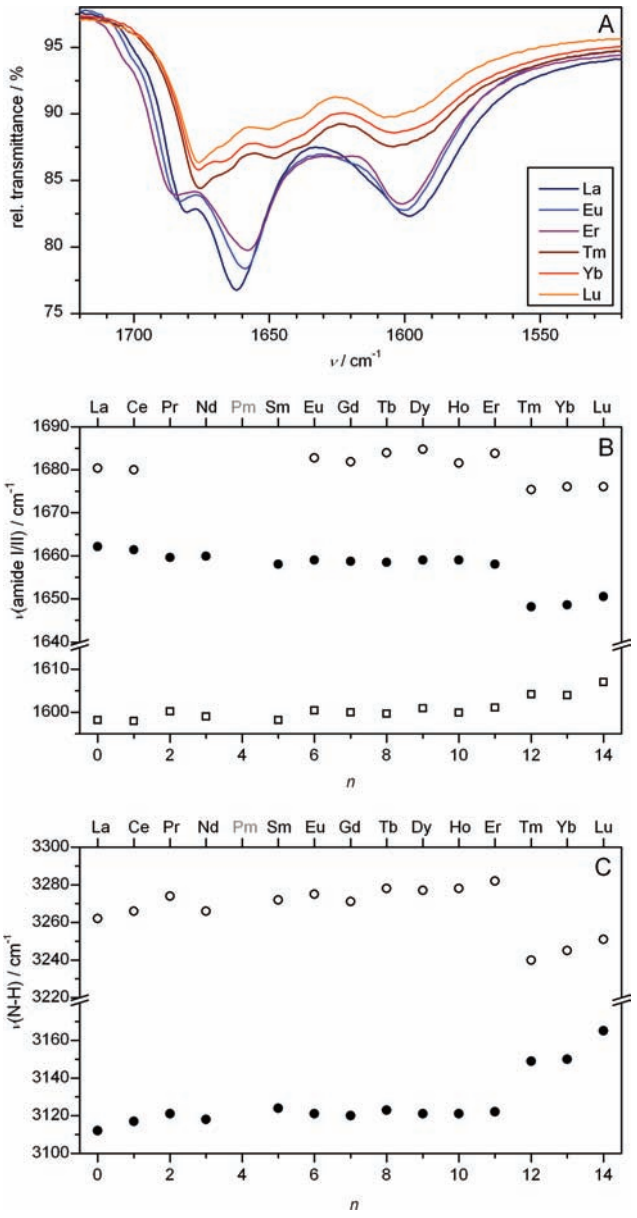


**Figure 3.** FT-IR spectroscopy data of the complexes $[Ln(ttham)]Cl_3 \cdot 3H_2O$: IR spectra of the complexes with Ln = La, Eu, Er, Tm, Yb, Lu in the region between 1720 and 1520 $cm^{-1}$ (A). Plot of the IR absorption maxima of all complexes (Ln = La−Lu, except Pm, represented by the number $n$ of their 4f electrons) in this amide I and II frequency range (B) and in the $\nu$(N−H) frequency range between 3300 and 3100 $cm^{-1}$ (C).

complexes is compared in Figure 3A. On the basis of the similarity of their spectral features, the compounds could be divided into two groups, which comprised the ttham complexes of La, Eu, and Er on the one side and those of Tm, Yb, and Lu on the other side. In fact, as evidenced from a more extended analysis, group one comprised all La−Er ttham complexes, exemplified by a comparison of the absorption maxima in the 1520−1720 $cm^{-1}$ range shown in Figure 3B. Here a single step shift of the absorption maxima, most pronounced in the spectral region 1645−1685 $cm^{-1}$, was recognized comparing the early lanthanides up to Er with those following and including Tm. A similar pronounced change of the absorption maxima in the $\nu$(N−H) frequency region was observed between the Er and Tm complexes as

(29) Seitz, M.; Oliver, A. G.; Raymond, K. N. *J. Am. Chem. Soc.* **2007**, *129*, 11153–11160.
(30) Quadrelli, E. A. *Inorg. Chem.* **2002**, *41*, 167–169.
(31) Abbasi, A.; Damian Risberg, E.; Eriksson, L.; Mink, J.; Persson, I.; Sandström, M.; Sidorov, Y. V.; Skripkin, M. Y.; Ullström, A.-S. *Inorg. Chem.* **2007**, *46*, 7731–7741.
(32) Mink, J.; Skripkin, M. Y.; Hajba, L.; Németh, C.; Abbasi, A.; Sandström, M. *Spectrochim. Acta A* **2005**, *61*, 1639–1645.

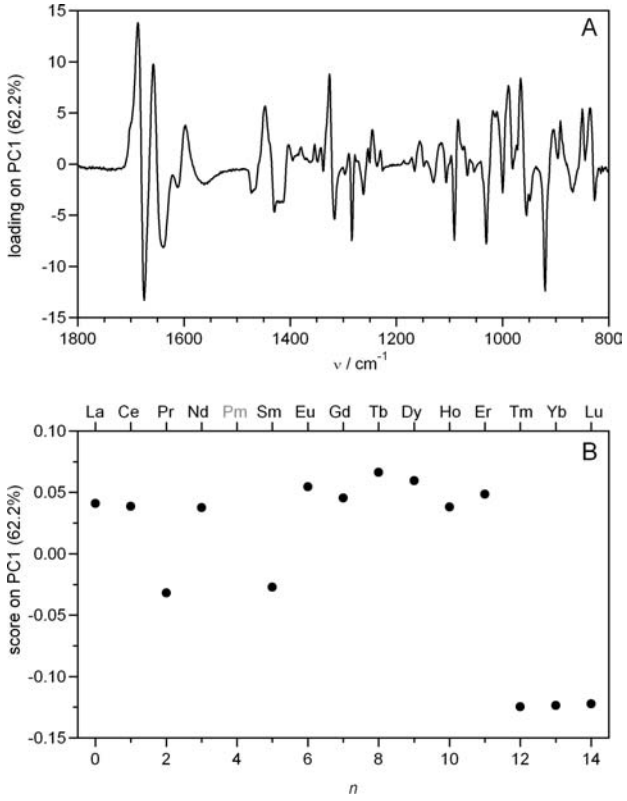


**Figure 4.** FT-IR spectroscopy data of the complexes $[Ln(ttham)]Cl_3 \cdot 3H_2O$ (Ln = La−Lu, except Pm, represented by the number *n* of their 4f electrons): Results of a principal component analysis of the IR spectra in the region 1800−800 $cm^{-1}$. Loadings on PC1 (62.24%) (A), scores on PC1 (62.24%) (B).

summarized in Figure 3C. The changes of these characteristic absorption bands indicated substantial structural differences between the Er and the Tm complex, whereas all earlier lanthanide complexes were concluded to form a group of structurally similar complexes and those following Tm to form a second such group.

Further evidence was obtained from a principal component analysis of the above spectra (Figure 4). Figure 4A shows the loadings on the first principal component (PC 1, accounting for 62.2% of the variance in the experimental data), in the fingerprint region 800−1800 $cm^{-1}$. The PC 1 scores of the different ttham complexes (Figure 4B) also underwent a single systematic change between the Er and Tm complexes and therewith confirmed the above conclusions drawn from comparing a few characteristic frequencies.

These differences were even more evident in the Raman spectra of the above complexes, which were analyzed in the same way (Figure 5). Here the most pronounced changes were found in the extended fingerprint region from 1720 down to 300 $cm^{-1}$ (Figures 5A and B), which in this case further included characteristic low frequency vibrations of the lanthanide-donor bonds in the first coordination sphere, and in the $\nu$(C−H) frequency region (Figures 5C and D). Overall the vibrational spectra of the ttham complexes demonstrated significant differences in the complete spectral range comparing the Tm, Yb, and Lu complexes with those of La to Er, which strongly suggested the occurrence of a fundamental structural change between the Er and Tm complexes.

The crystal structure analysis of $[Eu(ttham)](ClO_4)_3$, which is a representative example of the first group of ttham complexes, showed a 10-fold coordination of the ttham ligand to the $Eu^{3+}$ ion. It had been concluded earlier that $[Yb(ttham)]^{3+}$, a representative of the second group of ttham complexes, is best described as a 9-fold coordinated complex with one uncoordinated terminal acetamide group.[23] Hence, on the basis of the above vibrational spectroscopy data, the ttham complexes of La−Er were hypothesized to consist of 10-fold coordinated lanthanide ions completely wrapped by the decadentate ttham ligand, whereas those complexes of Tm−Lu comprise only 9-coordinate lanthanide ions.

To further test this hypothesis, IR spectra were measured of the $Eu^{3+}$ and $Tm^{3+}$ complexes of the nonadentate ligands 1bttpam and 4bttpam (Figures 6A and C, respectively). The complexes of both of these ligands exhibited only two strong, broad peaks in the 1520−1740 $cm^{-1}$ region, characteristic of the amide I and II vibrations. In both cases, the differences between the Eu and Tm complexes were very small, which indicated the absence of fundamental structural differences. In the case of the 1bttpam ligand, this has been substantiated by the crystal structure analysis results of both, the Eu and the Tm complexes, which for both trications confirmed a similar 9-fold coordination geometry, and hence strongly supported the above conclusions. The Eu and Tm complexes of 4bttpam were therefore also assumed to be structurally very similar, most likely comprising a 9-fold coordinated lanthanide ion.

The potentially decadentate ttha-tm$^{2-}$ ligand represents a more complex case. Here the studied $Eu^{3+}$ and $Tm^{3+}$ complexes were found to exhibit profoundly different IR spectra (Figure 6B), quite similar to the results obtained for the ttham complex series. This is indicative of a change in coordination number, which is therefore assumed to be 10 in the Eu complex and only 9 in the Tm complex, as will be further discussed below. The $Eu^{3+}$ and $Tm^{3+}$ complexes of the neutral, potentially decadentate $Bu_2$ttha-tm ligand, on the other hand, did not show such marked differences in their IR spectra and in this case fundamental structural differences are therefore unlikely (Figure 6D). These two $Bu_2$ttha-tm complexes are assumed to be 10-coordinate. A 10-coordinate is more likely than a 9-coordinate structure, considering the presumably longer Ln-donor bonds, because of a lower donor strength of the *tert*-butyl ester groups, which enlarge the first coordination sphere to allow for the accommodation of 10 donors even in the Tm complex.

**Electrochemistry.** Europium(II) is the most easily accessible divalent lanthanide ion with a formal redox potential of the aqua ion of $E_{1/2} = -0.63$ V (vs Ag/AgCl) in aqueous solution.[33,34] Nevertheless, the electrochemistry of Eu chelate complexes has just begun to be explored systematically in recent years, with the aim

(33) Cotton, S. *Lanthanide and Actinide Chemistry*; John Wiley & Sons: Chichester, U.K., 2006.
(34) Tóth, É.; Burai, L.; Merbach, A. E. *Coord. Chem. Rev.* **2001**, *216−217*, 363–382.

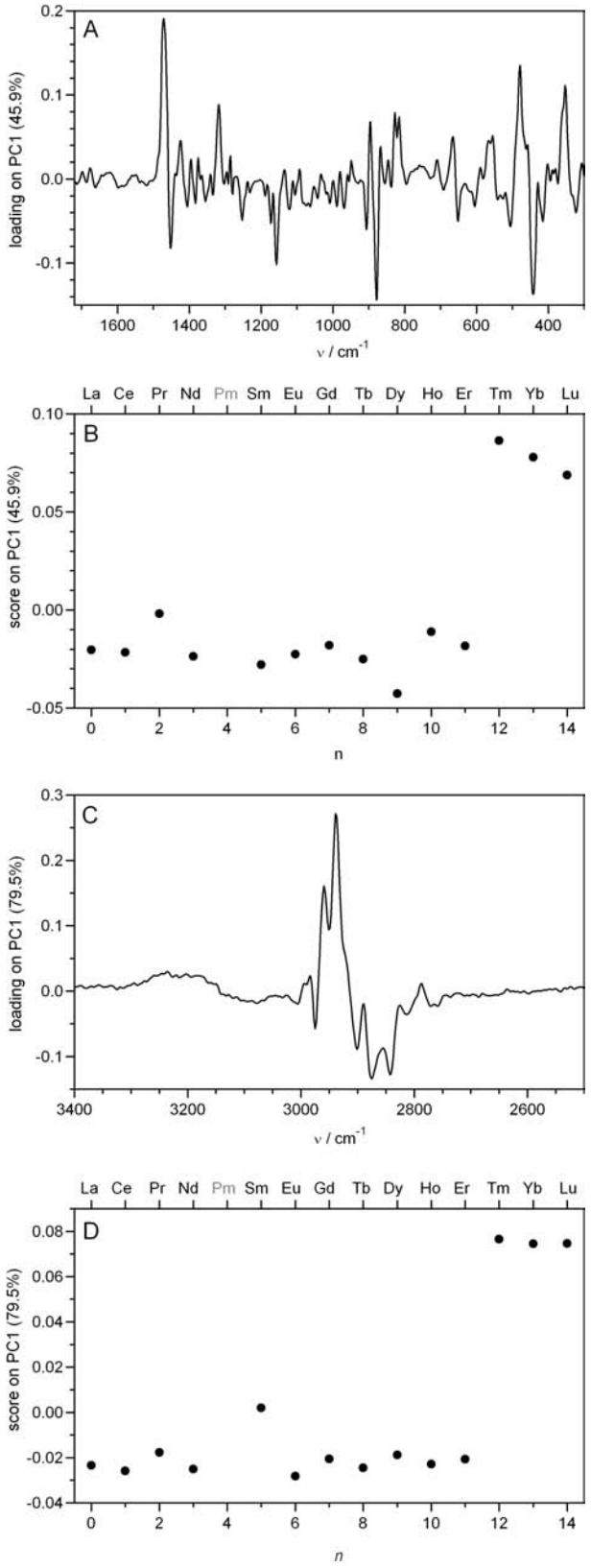


**Figure 5.** Raman spectroscopy data of the complexes $[Ln(ttham)]Cl_3 \cdot 3H_2O$ (Ln = La−Lu, except Pm, represented by the number *n* of their 4f electrons): Results of a principal component analysis of the Raman spectra in the region 1720−300 $cm^{-1}$ (A, B) and in the region 3400−2500 $cm^{-1}$. (C, D). Respective loadings (A, C) and scores (B, D) on PC1.

of developing redox-sensitive MRI CAs suitable of probing locally, for example, the partial oxygen pressure,

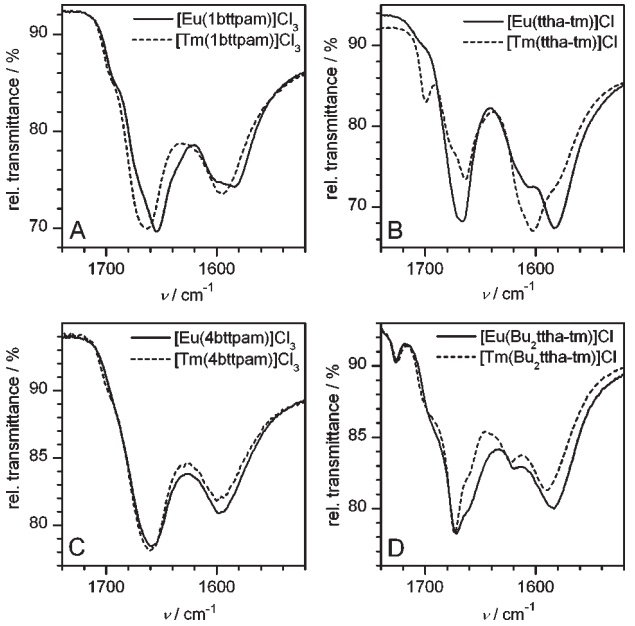


**Figure 6.** IR spectra of the complexes $[Ln(L)]Cl_n \cdot xH_2O$ (Ln = Eu, Tm; L = 1bttpam (A), ttha-$tm^{2-}$(B), 4bttpam (C), $Bu_2$ttha-tm(D)), in the amide I and II frequency range between 1740 and 1520 $cm^{-1}$.

which is relevant in various pathologies, such as strokes or tumors.[35−37]

From an analytical point of view, studying the electrochemical properties of a Eu complex provides information on the relative stability of its two relevant redox states, and hence on the structural parameters influencing those stabilities. With the aim of gaining such information, cyclovoltammetry measurements were conducted of the present Eu complexes in aqueous solution. The corresponding cyclovoltammograms are superimposed in Figure 7. The Eu complexes of the three neutral ligands ttham (red), 1bttpam (blue), and 4bttpam (green) all showed a reversible or quasi-reversible $Eu^{2+}/Eu^{3+}$ redox process with a formal half-potential ($E_{1/2}$) of about −0.9 V. Significant differences were nevertheless observed in the peak separation of the respective reduction and oxidation waves, which became more separated in the ligand order: ttham < 1bttpam < 4bttpam. These differences were most likely a result of the extension of the first coordination sphere upon reduction of the encapsulated $Eu^{3+}$ ion to the larger $Eu^{2+}$ ion. Whereas this transition seemed to cause only small structural changes in the already 10-fold coordinated ttham complex, in the case of the only 9-coordinate 1bttpam and 4bttpam complexes (in the latter even more pronounced) larger structural changes were assumed to result from an increased accessibility of the complex to a tenth ligand donor, most likely a water molecule, getting in closer contact with the sterically less protected $Eu^{2+}$ ion. It must further be considered that the different conformers known to exist in aqueous solutions of 4bttpam complexes may stabilize the two redox states to a different degree and may therefore require

(35) Seibig, S.; Tóth, É.; Merbach, A. E. *J. Am. Chem. Soc.* **2000**, *122*, 5822–5830.
(36) Burai, L.; Tóth, É.; Seibig, S.; Scopelliti, R.; Merbach, A. E. *Chem.—Eur. J.* **2000**, *6*, 3761–3770.
(37) Botta, M.; Ravera, M.; Barge, A.; Bottaro, M.; Osella, D. *Dalton Trans.* **2003**, 1628–1633.

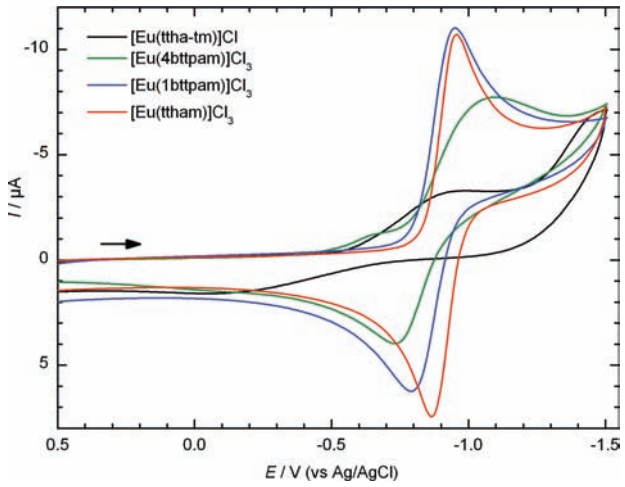


**Figure 7.** Cyclovoltammograms of complexes $[Eu^{III}(L)]Cl_n$ (L = ttham (red), 1bttpam (blue), or 4bttpam (green) and $n = 3$; or L = ttha-$tm^{2-}$ (black) and $n = 1$) in water (0.1 M $NaNO_3$, pH 7.40), glassy carbon working electrode, scan rate 0.1 $V \cdot s^{-1}$. Electrochemical data (all data vs Ag/AgCl) ligand ($E_{1/2}$/V, $\Delta E$/V): ttham (−0.91, 0.09), 1bttpam (−0.88, 0.16), 4bttpam (−0.91, 0.36), ttha-$tm^{2-}$ (−, 0.94).

ligand reorientation reactions accompanying the redox process.[23,38] The involvement of any of these processes can explain the contribution of a reversible chemical component in addition to the redox process causing its overall quasi-reversible electrochemical character.

An extreme case in this respect is the Eu complex of the dianionic ttha-$tm^{2-}$ ligand, which was characterized by an electrochemically irreversible reduction process with an observed reduction potential ($E_{red}$) of about −0.98 V and a peak separation ($\Delta E$) as large as 0.94 V (at a scan rate of 0.1 $V \cdot s^{-1}$, black curve). The reduction process occurred at a slightly more negative potential compared to the above three tricationic complexes, which could be related to the negative charge of the ttha-$tm^{2-}$ ligand stabilizing the $Eu^{3+}$ relative to the $Eu^{2+}$ state. Nevertheless, on the basis of pure charge considerations, a larger negative shift of the reduction potential was expected. The large peak separation, on the other hand, provided evidence for a structural change upon $Eu^{3+} \rightarrow Eu^{2+}$ reduction. Considering the above deduced structural proposal of a 10-fold coordinated $[Eu^{III}(ttha\text{-}tm)]^+$ complex, a change of the coordination number was not expected upon reduction, which is known to even reduce the steric hindrance in the first coordination sphere. It can therefore be assumed that rather an unfavorable steric crowding in the $Eu^{3+}$ complex caused the reoxidation of a sterically more relaxed Eu(II) complex to become kinetically hindered, resulting in the significant positive peak shift of the oxidation peak to about −0.05 V. An exceptionally good geometric fit of the ttha-$tm^{2-}$ ligand with the preferences of the $Eu^{2+}$ ion may indeed also explain the unexpectedly low reduction potential of this complex compared to those of the three neutral ligands.

**NMR Spectroscopy.** Water-suppressed $^1H$ NMR spectra of the above compounds were measured in aqueous buffer solution at pH 2.7 (red lines) and 7.4 (blue lines). Figure 8 shows spectra of the europium(III) complexes of ttham, 1bttpam, 4bttpam, and ttha-$tm^{2-}$ at 310 K. At pH 7.4 the exchange reaction of the amide protons with solvent water was fast. Therefore, their NMR resonances were relatively broad and, in addition, easily saturated by the pre-saturation pulse used for water suppression via the hydrogen exchange reaction.[39] They became detectable, however, at pH 2.7, where the base-catalyzed exchange reaction was sufficiently slow.

The spectrum of $[Eu(ttham)]^{3+}$ at pH 7.4 (Figure 8A) was characterized by some 10 overlapping, intermediately broad peaks (line widths: 20−200 Hz) corresponding to the expected number of 24 C−H protons. The small number of peaks indicated that the approximate $C_2$-symmetry of the 10-fold coordinated complex observed in its crystal structure was maintained in aqueous solution. Some 8 additional resonances (indicated by arrows) could be ascribed to exchangeable amide protons based on the pH 2.7 spectrum.

The C−H resonances of the nonadentate ligands 1bttpam and 4bttpam in their respective Eu complexes were both spread over an almost twice as wide chemical shift range (about −20 to 20 ppm, Figure 8, panels B and C). The larger lanthanide-induced shifts reflected the smaller distances between the methylene protons of the ligand and the Eu ion in the nonadentate complexes. Whereas in the case of the 1bttpam ligand these peaks could be ascribed to a single set of the 29 expected protons at pH 7.4, the larger number of peaks with a wide range of intensities found for the 4bttpam complex indicated the presence of more than one conformer in solution. The same conclusions had been drawn earlier for the Yb complexes of these two ligands, for which comparable difference in their $^1H$ NMR spectra had been observed, as well as for the lanthanide complexes of the related $ttha^{6-}$ ligand ($ttha^{6-}$ = triethylenetetramine-*N*,*N*,*N*′,*N*″,*N*‴,*N*‴-hexaacetate) and its terminal bis(amide) derivative, which had been studied in great detail.[23,40,41] In the low-pH spectrum of $[Eu(4bttpam)]^{3+}$ only 3 of the expected 10 peaks could be ascribed to exchangeable protons, whereas 9 peaks were identified in the structurally better defined 1bttpam complex.

The $^1H$ NMR spectra of $[Eu(ttha\text{-}tm)]^+$ shown in Figure 8D exhibited the characteristics of those of the respective ttham complex (Panel A) in terms of chemical shift range, the overall number of peaks, and the resonances of the exchangeable protons, and they did not resemble the spectral features of the two 9-fold coordinated complexes (Panels B and C). This strongly indicated that the Eu complexes of the two potentially decadentate ligands adopted very similar structures in solution, which were characterized by a 10-fold coordination of the europium ion.

Figure 9 shows the $^1H$ NMR spectra of the respective $Tm^{3+}$ complexes of the above ligands. Generally, as expected, the resonances of all Tm complexes were observed in a much larger chemical shift range spanning up

(38) Dunand, F. A.; Aime, S.; Merbach, A. E. *J. Am. Chem. Soc.* **2000**, *122*, 1506–1512.

(39) Connelly, G. P.; Bai, Y.; Jeng, M.-F.; Englander, S. W. *Proteins: Struct., Funct., Genet.* **1993**, *17*, 87–92.

(40) Lee, S.-G. *Magn. Reson. Chem.* **2000**, *38*, 820–822.

(41) Zitha-Bovens, E.; Muller, R. N.; Laurent, S.; Vander Elst, L.; Geraldes, C. F. G. C.; van Bekkum, H.; Peters, J. A. *Helv. Chim. Acta* **2005**, *88*, 618–632.

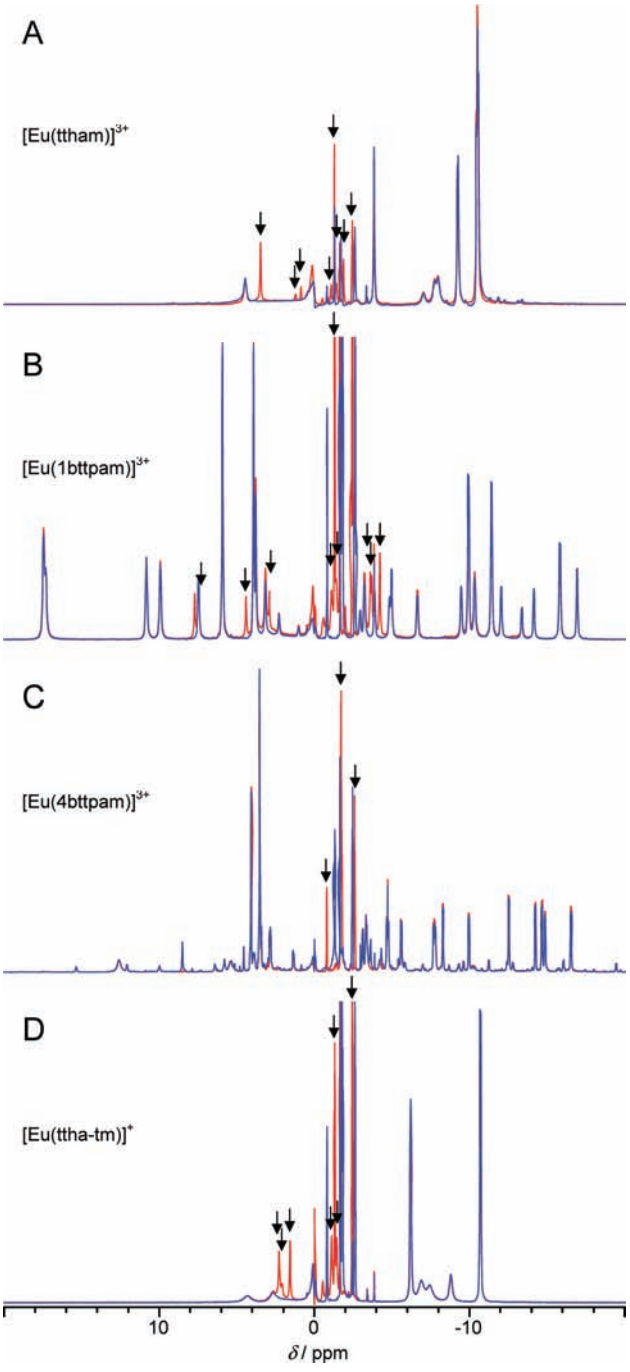


**Figure 8.** $^1$H NMR spectra of $[Eu(ttham)]^{3+}$ (A), $[Eu(1bttpam)]^{3+}$ (B), $[Eu(4bttpam)]^{3+}$ (C), and $[Eu(ttha\text{-}tm)]^{+}$ (D) in aqueous solution ($c$([Eu(L)]Cl$_n$) = 20 mM, $c$(MOPS) = 20 mM, $T$ = 310 K, $B_0$ = 7 T) at two pH values (7.40 (blue), 2.70 (red)). The water signal was suppressed by application of a continuous-wave presaturation pulse (1.5 s, 10 $\mu$T). Chemical shifts ($\delta$) are relative to the resonance frequency of water ($\delta$ = 0 ppm). The resonances of exchangeable protons are indicated by arrows.

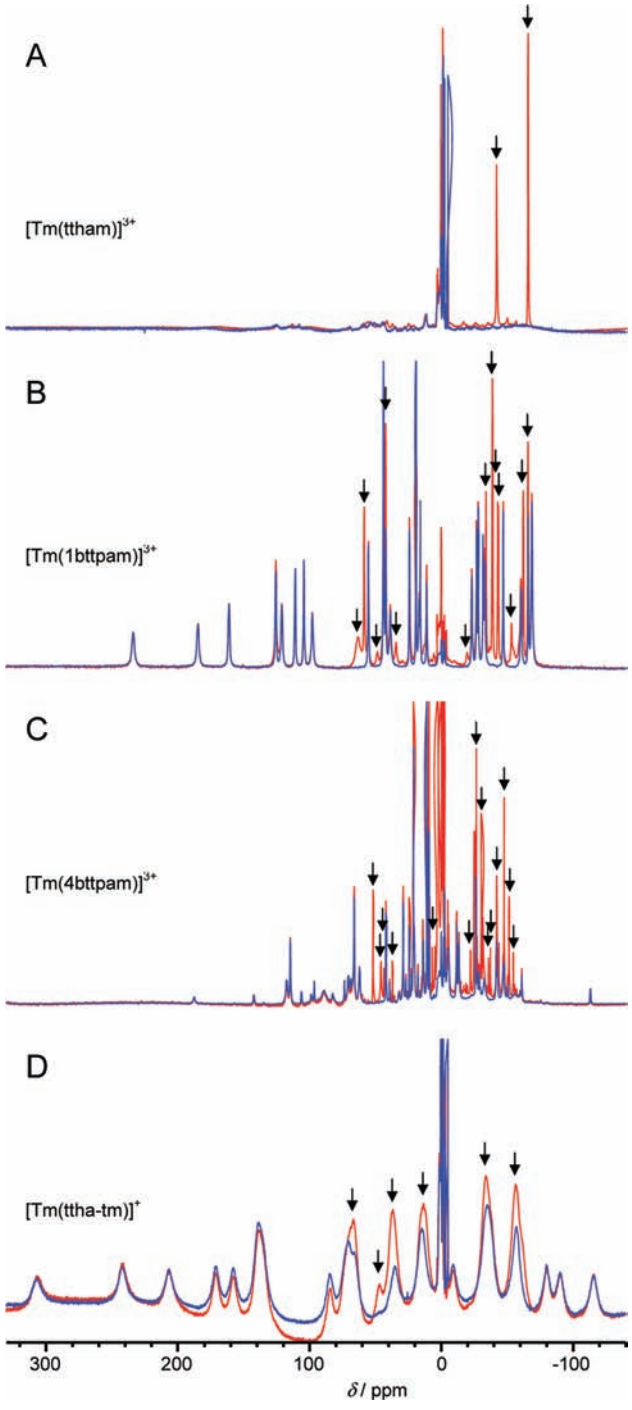


**Figure 9.** $^1$H NMR spectra of $[Tm(ttham)]^{3+}$ (A), $[Tm(1bttpam)]^{3+}$ (B), $[Tm(4bttpam)]^{3+}$ (C), and $[Tm(ttha\text{-}tm)]^{+}$ (D) in aqueous solution ($c$([Tm(L)]Cl$_n$) = 20 mM, $c$(MOPS) = 10 mM, $T$ = 310 K, $B_0$ = 7 T) at two pH values (7.40 (blue), 2.70 (red)). The water signal was suppressed by application of a continuous-wave presaturation pulse (1.5 s, 10 $\mu$T). Chemical shifts ($\delta$) are relative to the resonance frequency of water ($\delta$ = 0 ppm). The resonances of exchangeable protons are indicated by arrows.

to more than 400 ppm. Apart from this, comparing first the Eu and Tm complexes of the nonadentate ligands 1bttpam and 4bttpam, very similar spectral characteristics could be noticed within each ligand group, indicative of similar solution structures (Panels B and C in Figures 8 and 9). In all four cases, peaks ascribed to exchangeable protons appeared in the positive as well as the negative chemical shift range. Both 1bttpam complexes exhibited a single set of C−H resonances, whereas both 4bttpam compounds showed a larger number of peaks, which were ascribed to the presence of more than one conformer, as discussed above.

A special situation was encountered when studying the $^1$H NMR properties of $[Tm(ttham)]^{3+}$ (Figure 9A). At pH 7.4 all proton resonances were found to be extremely broad, making them almost undetectable. In contrast,

the spectrum measured at pH 2.7 was characterized by two additional, significantly sharper peaks at −40 and −65 ppm, indicative of exchangeable protons. In fact, the appearance of comparably sharp $^1$H NMR peaks at pH 2.7, which we generally ascribed to exchangeable protons, even in the absence of well-defined C−H resonances, was observed for the majority of the ttham complexes $[Ln(ttham)]^{3+}$ (Ln = La−Lu; see the Supporting Information, Figures S1−S5).

For the Gd complex, the observed extensive line broadening (fast $T_2$ relaxation) was expected, because of the long electron relaxation times of the $Gd^{3+}$ ion.[42,43] The line broadening in the spectra of the other $Ln^{3+}$ complexes, however, could only be explained by exchange phenomena related to the conformational mobility of the ttham ligand.[43,44] A geometric analysis revealed that up to three diastereomeric isomer pairs are possible in a 9-fold coordinated ttham complex.[41] Although we found an approximate $C_2$-symmetric coordination geometry in the crystal structure of the 10-coordinate Eu complex $[Eu(ttham)]^{3+}$, it is possible that the 10-fold coordinated ttham complexes in solution exhibited a lower symmetry. This allowed for the formation of a larger number of isomers also of those complexes that were in a dynamic equilibrium situation, in which the conformational changes occurred at a rate that roughly corresponded to the chemical-shift separation between the conformers.[44] The rate of conformational change reactions generally depends on the detailed structure of the involved complexes, hence on the exchange reaction pathways, as well as on the size of the lanthanide ion, which determines the amount of geometrical strain built into the respective structures.[40,45,46]

The striking appearance of sharp signals only for the amide protons is consistent with this picture. The signals of these protons were in part broadened because of conformational exchange, too, but in addition they exchanged on a longer time scale (comparable to $T_2$* of the bulk water) with the bulk water protons, which were characterized by a much narrower resonance line. The expected line width of the exchangeable-proton signals was, therefore, the weighted average of the small fraction of bound protons with severe line broadening and of a large fraction of bulk water protons with a relatively narrow line width.[47]

These relatively sharp resonances of the exchangeable protons of the $[Ln(ttham)]^{3+}$ series were therefore used to obtain additional structural information. We determined the lanthanide induced shift (LIS) of the most highly shifted exchangeable protons ($\delta'$), since those could be identified most accurately for all ttham complexes. The LIS was obtained from the observed chemical shift ($\delta$) after correction for the diamagnetic contribution ($\delta_{dia}$), which was estimated as the respective chemical shift value of the diamagnetic complex $[La(ttham)]^{3+}$ (eq 2, Supporting Information, Table S1).[48]

$$\delta' = \delta - \delta_{dia} = \delta_c + \delta_p \quad (2)$$

The remaining contact ($\delta_c$) and pseudocontact shift ($\delta_p$) contributions can be factorized (eq 3).[48]

$$\delta' = F \cdot \langle S_Z \rangle + G \cdot C^D \quad (3)$$

The factors $\langle S_Z \rangle$ and $C^D$ are characteristic of the lanthanide ion and independent of the ligand, whereas $F$ and $G$ are metal-independent constants characteristic of the specific NMR nucleus. Upon rewriting, eq 4 is obtained.

$$\frac{\delta'}{\langle S_Z \rangle} = F + G \cdot \frac{C^D}{\langle S_Z \rangle} \quad (4)$$

Under the precondition that no structural change of the complex occurs across the lanthanide series, a straight line should therefore be obtained in a plot of $\delta'/\langle S_Z \rangle$ versus $C^D/\langle S_Z \rangle$.

In the ttham series a linear plot was indeed obtained for the lanthanides Ce−Er, whereas the Tm and Yb complexes defined a second group that was clearly separated from the other compounds (Figure 10). This result indicated that also in solution the Ce−Er complexes of ttham maintained the same structural motif, whereas the Tm and Yb complexes were structurally different from those. Taking into account the earlier discussed results, it was concluded that the 10-fold coordination found for the ttham complexes of the lanthanides up to Er was conserved in solution. The structural change that occurred upon moving to Tm and Yb was concluded to result in a coordination number of 9 for those late lanthanides in the solid state as well as in solution.

Equation 3 may alternatively be rewritten to obtain eq 5.

$$\frac{\delta'}{C^D} = F \cdot \frac{\langle S_Z \rangle}{C^D} + G \quad (5)$$

A plot of $\delta'/C^D$ versus $\langle S_Z \rangle/C^D$ did not reveal any linear correlation (Supporting Information, Figure S6). It had been noted that eq 3 should be used when experimental shifts are largely dipolar in origin, whereas eq 5 should be more suitable when contact contributions predominate.[49] This suggested that the observed LIS of the exchangeable amide protons of the ttham complexes was dominated by pseudocontact shift contributions, as will be further discussed below.

Returning to Figure 9, the NMR spectra of $[Tm(ttha-tm)]^+$ (Panel D) were better defined compared to $[Tm(ttham)]^{3+}$ (Panel A), but still characterized by fairly broad peaks (line widths up to 3000 Hz). In contrast to the respective Eu complexes, the lanthanide-induced shifts of $[Tm(ttha-tm)]^+$ were even larger than those of $[Tm(1bttpam)]^+$. This suggested that the complex $[Tm(ttha-tm)]^+$ in solution, like in the solid state, was nonadentate. The respective distances between the methylene protons of the ligand and the $Tm^{3+}$ ion in the nonadentate $[Tm(ttha-tm)]^+$ complex were expected to be shorter than those in the nonadentate $[Tm(1bttpam)]^+$

(42) Geraldes, C. F. G. C.; Urbano, A. M.; Alpoim, M. C.; Sherry, A. D.; Kuan, K.-T.; Rajagopalan, R.; Maton, F.; Muller, R. N. *Magn. Reson. Imaging* **1995**, *13*, 401–420.
(43) Peters, J. A. *Inorg. Chem.* **1988**, *27*, 4686–4691.
(44) Holz, R. C.; Horrocks, W. D.Jr. *Inorg. Chim. Acta* **1990**, *171*, 193–198.
(45) Uggeri, F.; Aime, S.; Anelli, P. L.; Botta, M.; Brocchetta, M.; de Haën, C.; Ermondi, G.; Grandi, M.; Paoli, P. *Inorg. Chem.* **1995**, *34*, 633–642.
(46) Frullano, L.; Rohovec, J.; Peters, J. A.; Geraldes, C. F. C. G. *Top. Curr. Chem.* **2002**, *221*, 25–60.
(47) Bertini, I.; Luchinat, C. *Coord. Chem. Rev.* **1996**, *150*, 77–110.
(48) Peters, J. A.; Huskens, J.; Raber, D. J. *Prog. Nucl. Magn. Reson. Spectrosc.* **1996**, *28*, 283–350.
(49) Singh, M.; Reynolds, J. J.; Sherry, A. D. *J. Am. Chem. Soc.* **1983**, *105*, 4172–4177.

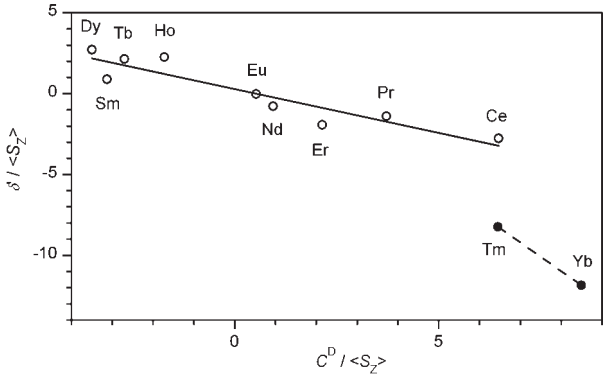


**Figure 10.** LIS of the most highly shifted amide protons ($\delta'$) of the complexes $[Ln(ttham)]^{3+}$ (Ln = Ce−Yb, except Pm) in aqueous buffer solution ($c$(MOPS) = 10 mM, pH 2.70, 310 K, 7 T) plotted as $\delta'/\langle S_Z\rangle$ as a function of the term $C^D/\langle S_Z\rangle$, which is characteristic of the shift-inducing properties of the respective metal ions.[48] The LIS was obtained from the observed chemical shift ($\delta$) after correction for the diamagnetic contribution ($\delta_{dia}$) as derived from the respective peak of the diamagnetic complex $[La(ttham)]^{3+}$ ($\delta' = \delta - \delta_{dia}$, $\delta_{dia} = 3.70$ ppm, $\delta_{H2O} = 0$ ppm). Linear regression analysis: Series 1 (La = Ce−Er), $\delta'/\langle S_Z\rangle = 0.29-0.54(C^D/\langle S_Z\rangle)$, $R = 0.93$ ($N = 9$); Series 2 (La = Tm−Yb), $\delta'/\langle S_Z\rangle = 3.17-1.77(C^D/\langle S_Z\rangle)$, $N = 2$.

and $[Tm(4bttpam)]^+$ complexes because of the negative charge of the tta-$tm^{2-}$ ligand.

Although some of the resonances of the $[Tm(tta\text{-}tm)]^{3+}$ complex appeared slightly more intense at pH 2.7 than at pH 7.4, they did not become significantly sharper. In this regard they did thus not resemble the amide signals of $[Tm(ttham)]^{3+}$. This difference was most likely a consequence of the different charge of the two ligands, which was expected to influence the relative stability of different conformers and to slow down their conversion rate in case of the presumably more strongly bound tta-$tm^{2-}$ ligand.

**Proton Longitudinal Relaxivity Measurements.** From the measured longitudinal relaxation times ($T_{1,obs}$) of solutions of the above Tm complexes, water proton relaxivity values $r_1$ were determined according to eq 6 (Table 2), after correction for diamagnetic contributions measured in pure buffer solution ($T_{1,dia} = T_{1,buffer}$).

$$r_1 = \frac{(T_{1,obs}^{-1} - T_{1,dia}^{-1})}{c(\text{complex})} \tag{6}$$

The longitudinal relaxivity increased in the following order of ligands: 1bttpam < ttham ∼ tta-$tm^{2-}$ < 4bttpam, with the complexes of the two nonadentate ligands representing the extreme cases. All evidence so far indicated that $[Tm(1bttpam)]^{3+}$ was indeed the structurally best defined complex of this series. The Tm ion was completely and stably encapsulated by the nonadentate ligand, and the complex did not bear water ligands in its first coordination sphere. Hence, when neglecting outer-sphere effects, mainly second-sphere contributions to its relaxivity were expected. The Tm complexes of ttham and tta-$tm^{2-}$ were both structurally more flexible with respect to the four terminal acetamide donors, of which the three coordinated acetamides were in a fast exchange equilibrium with the dangling fourth donor. An expected consequence of this exchange process was a transiently closer interaction of the encapsulated Tm ion with the solvent water causing a slightly increased relaxivity. This effect seemed to be even more pronounced in the case of $[Tm(4bttpam)]^{3+}$, which according to the above-discussed evidence was involved in a similar exchange reaction involving different coordination conformers, however, offering a maximum of only nine donor groups, which on average provided less shielding of the encapsulated ion against the solvent water than the decadentate ligands. The same relaxivity trend had indeed been found earlier for the complexes $[Yb(L)]^{3+}$ (L = 1bttpam, ttham, 4bttpam).[23]

**Table 2.** Proton Relaxivities of the Tm Complexes $[Tm(L)]^{n+}$ in Aqueous Buffer Solution[a]

| ligand (L) | $T_{1,obs}$ /s | $r_1$[b] /$10^{-3}$ $mM^{-1}\cdot s^{-1}$ |
|---|---|---|
| ttham | 1.17 | 31 |
| 1bttpam | 1.33 | 26 |
| 4bttpam | 0.97 | 40 |
| tta-$tm^{2-}$ | 1.10 | 34 |

[a] $c$(MOPS) = 10 mM, pH 7.40, 310 K, 7 T. [b] Calculated as $r_1 = [(1/T_{1,obs}) - (1/T_{1,buffer})]/c([Tm(L)]Cl_n)$, $c([Tm(L)]Cl_n) = 20$ mM, $T_{1,buffer} = 4.34$ s.

Within the ttham series, the longitudinal relaxivity ($r_1$) of all lanthanide complexes varied consistently (Figure 11A), with the expected exception of $[Gd(ttham)]^{3+}$ ($r_1 = 1.22$ $mM^{-1}\cdot s^{-1}$), which showed an approximately 15 times higher relaxivity than the complexes of its three heavier neighbors. A switch of the coordination number from 10 to 9 when moving from Er to Tm was not reflected within these data. This is consistent with the relaxivities of the $[Tm(L)]^{3+}$ series (Table 2), which differed by less than 20% comparing the 10-coordinate ttham with the 9-coordinate 1bttpam complex. It could therefore be assumed that the relaxivity of all here discussed complexes was predominantly determined by second sphere contributions because of the lack of water ligands in the first coordination sphere.[50,51]

A qualitative assessment revealed the relaxivity change across this series to correlate with the square of the magnetic moment of the bound lanthanide trication, as was expected for contributions from predominantly dipolar mechanisms in the second coordination sphere to the relaxation process, if hyperfine contributions were absent. For the ttham complexes in solution, strong interactions between water molecules of the second coordination sphere and the coordinated ligand are most likely, mainly assuming extensive hydrogen bonding of water oxygen atoms to the ttham amide protons as observed in the crystal structure of $[Eu(ttham)](ClO_4)_3$. Considering therefore second-sphere contributions only, the paramagnetic contribution to the relaxation rate ($1/T_{1,M}$) can be described by eq 7.[48,52,53]

$$\frac{1}{T_{1,M}} = \left[\frac{4}{3}\left(\frac{\mu_0}{4\pi}\right)^2 \gamma_I^2 \mu_B^2 \frac{T_{1,e}}{r^6}\right]\left(\frac{\mu}{\mu_B}\right)^2 + \left[\frac{6}{5}\left(\frac{\mu_0}{4\pi}\right)^2 \frac{\gamma_I^2 B_0^2 \mu_B^4}{(3kT)^2}\frac{1}{r^6}\left(\frac{\tau_R}{1+\omega_I^2\tau_R^2}\right)\right]\left(\frac{\mu}{\mu_B}\right)^4 \tag{7}$$

(50) Botta, M. *Eur. J. Inorg. Chem.* **2000**, 399–407.
(51) Tóth, É.; Helm, L.; Merbach, A. E. *Top. Curr. Chem.* **2002**, *221*, 61–101.
(52) Bertini, I.; Capozzi, F.; Luchinat, C.; Nicastro, G.; Xia, Z. *J. Phys. Chem.* **1993**, *97*, 6351–6354.
(53) Piguet, C.; Geraldes, C. F. G. C. Paramagnetic NMR lanthanide induced shifts for extracting solution structures. In *Handbook on the Physics and Chemistry of Rare Earths*; Bünzli, J.-C., Gschneidner, K. A., Eds.; Elsevier: North-Holland, 2003; Vol. 33, pp 353−463.

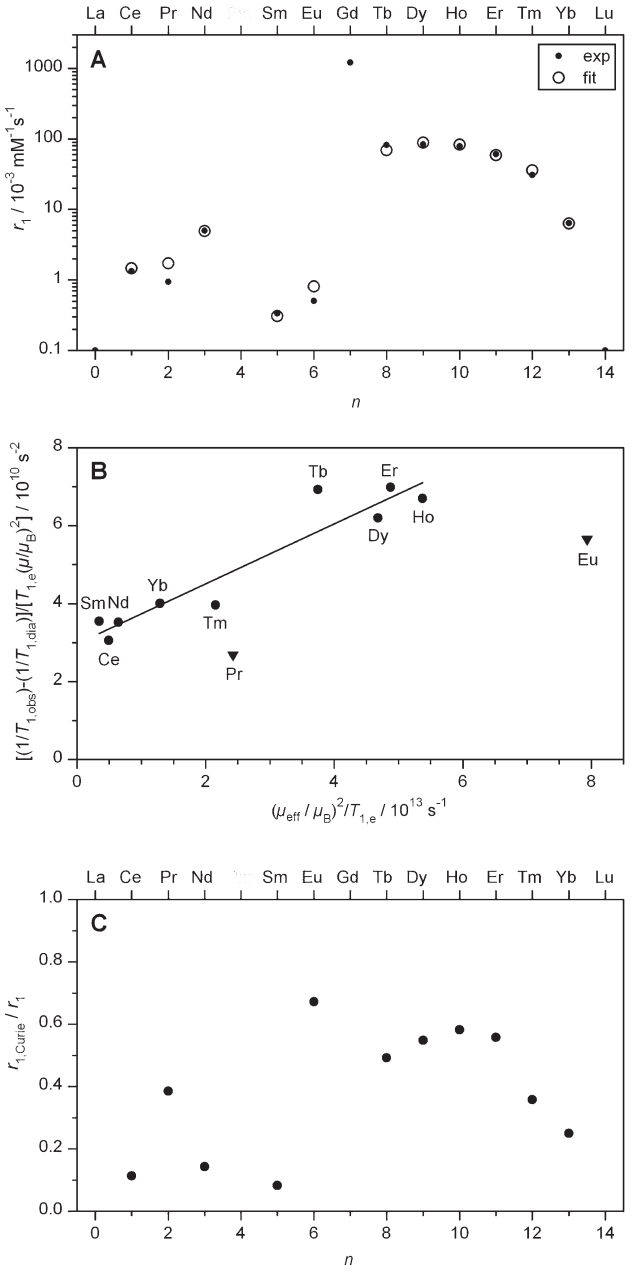


**Figure 11.** Proton relaxivities $r_1$ of the complexes $[Ln(ttham)]^{3+}$ (Ln = La−Lu, except Pm) in aqueous buffer solution ($r_1 = [(1/T_{1,obs}) - (1/T_{1,dia})]/c([Ln(ttham)]Cl_3)$, $c([Ln(ttham)]Cl_3)$ = 20 mM, $(T_1)_{dia}$ = 4.14 s ($[La(ttham)]Cl_3$), $c$(MOPS) = 10 mM, pH 7.40, $T$ = 310 K, $B_0$ = 7 T, closed circles) as a function of the complexed lanthanide ion ($Ln^{3+}$) as represented by the number $n$ of their 4f electrons. (A). Plot $(T_{1,obs}^{-1} - T_{1,dia}^{-1})/[T_{1,e}\cdot(\mu/\mu_B)^2]$ vs $(\mu/\mu_B)^2/T_{1,e}$ and linear regression analysis (Equations 11 and S1): $X = 2.97\cdot10^{10}$ $s^{-2}$, $Y = 7.68\cdot10^{-5}$ $s^{-1}$ ($N$ = 9 (not Ln = Pr, Eu), $R$ = 0.95) (B). Contribution of the Curie mechanism to the overall relaxivity, plotted as $r_{1,Curie}/r_1$ vs $n$ ($r_{1,Curie} = Y/c$(complex)$\cdot(\mu/\mu_B)^4$) (C).

In this equation the two main dipolar contributions are represented. The first term covers the "classical" dipolar contribution due to random fluctuations of the electronic field, and the second term describes the Curie relaxation, which arises from the interaction of the nuclear spin with the thermal average of the electronic spin. Here, $\mu_0/4\pi$ is the magnetic constant, $\gamma_I$ is the gyromagnetic ratio of the $^1H$ atom, $\mu_B$ is the Bohr magneton, $T_{1,e}$ is the electron spin relaxation time, $r$ is the distance between the considered $^1H$ nucleus and the lanthanide ion, $\mu$ is the effective magnetic moment of the lanthanide trication, $B_0$ is the magnetic field, $k$ is the Boltzmann constant, $T$ is the temperature, $\omega_I$ is the Larmor frequency of the $^1H$ nucleus, and $\tau_R$ is the rotational tumbling time of the complex.

In our analysis we considered only the dominant second-sphere relaxation mechanisms described by eq 7. The paramagnetic contribution ($T_{1,M}$) can be obtained from the measured relaxation times ($T_{1,obs}$) using eq 8.[6,48,52]

$$\frac{1}{T_{1,\mathrm{obs}}} = \frac{n_w \cdot c_{Ln}}{c_w} \cdot \frac{1}{T_{1,M} + \tau_M} + \frac{1}{T_{1,\mathrm{dia}}} \qquad (8)$$

Here, $n_w$ is the number of second-sphere water molecules engaged in dipolar interactions with the lanthanide nucleus, $c_{Ln}$ and $c_w$ are the concentrations of complex and water, respectively, and $\tau_M$ is the residence time of water molecules in the second coordination sphere. It is safe to assume that $\tau_M \ll T_{1,M}$ because of very fast exchange in the second coordination sphere. Thus eq 9 is obtained.

$$\frac{1}{T_{1,M}} = \frac{c_w}{c_{Ln}} \cdot \left(\frac{1}{T_{1,\mathrm{obs}}} - \frac{1}{T_{1,\mathrm{dia}}}\right) \cdot \frac{1}{n_w} \qquad (9)$$

Combining eqs 7 and 9 yields

$$\frac{c_w}{c_{Ln}} \cdot \left(\frac{1}{T_{1,\mathrm{obs}}} - \frac{1}{T_{1,\mathrm{dia}}}\right) \cdot \frac{1}{n_w} = \left[\frac{4}{3}\left(\frac{\mu_0}{4\pi}\right)^2 \gamma_I^2 \mu_B^2 \frac{T_{1,e}}{r^6}\right]\left(\frac{\mu}{\mu_B}\right)^2 + \left[\frac{6}{5}\left(\frac{\mu_0}{4\pi}\right)^2 \frac{\gamma_I^2 B_0^2 \mu_B^4}{(3kT)^2}\frac{1}{r^6}\left(\frac{\tau_R}{1+\omega_I^2\tau_R^2}\right)\right]\left(\frac{\mu}{\mu_B}\right)^4 \qquad (10)$$

The dipolar contribution in the first term depends on the electron spin relaxation time $T_{1,e}$, which varies considerably across the lanthanide series. Upon rewriting, eq 11 is obtained, according to which a linear correlation is expected in a plot $(T_{1,obs}^{-1} - T_{1,dia}^{-1})/[T_{1,e}\cdot(\mu/\mu_B)^2]$ versus $(\mu/\mu_B)^2/T_{1,e}$.

$$\frac{(T_{1,\mathrm{obs}}^{-1} - T_{1,\mathrm{dia}}^{-1})}{T_{1,e}\cdot(\mu/\mu_B)^2} = \left[\frac{4}{3}\left(\frac{\mu_0}{4\pi}\right)^2 \gamma_I^2 \mu_B^2 \frac{c_{Ln}}{c_w}\frac{n_w}{r^6}\right] + \left[\frac{6}{5}\left(\frac{\mu_0}{4\pi}\right)^2 \frac{\gamma_I^2 B_0^2 \mu_B^4}{(3kT)^2}\frac{c_{Ln}}{c_w}\frac{n_w}{r^6}\left(\frac{\tau_R}{1+\omega_I^2\tau_R^2}\right)\right]\frac{(\mu/\mu_B)^2}{T_{1,e}} \qquad (11)$$

This plot and the result of a linear regression analysis are shown in Figure 11B (for more details see the Supporting Information, eqs S1−S3). In the analysis, $T_{1,e}$ values as determined by Alsaadi et al. for diethylenetriamine-$N,N,N',N'',N''$-pentaacetate ($dtpa^{5-}$) complexes of the lanthanide series and $(\mu/\mu_B)^2$ values of the $Ln^{3+}$ aquo complexes were used.[54,55] Besides the Gd complex,

(54) Alsaadi, B. M.; Rossotti, F. J. C.; Williams, R. J. P. *J. Chem. Soc., Dalton Trans.* **1980**, 2151–2154.
(55) Gysling, H.; Tsutsui, M. *Adv. Organomet. Chem.* **1970**, *9*, 361–395.

the two lanthanides with very small $T_{1,e}$ values ($Pr^{3+}$ and $Eu^{3+}$) were omitted from the linear regression analysis. From the fit parameters, $\tau_R$ was calculated to be 2421 or 116 ps (see Supporting Information) of which the latter falls in the expectation range of 60−300 ps.[41] The true value for $\tau_R$ is therefore concluded to be 116 ps.

Since the remaining two parameters, the $^1$H−Ln distance $r$ and the number of respective water molecules $n_w$, are not independent variables, a numerical value could only be obtained for the term $(n_w/r^6)_{sol}$, which was determined to be $1.01 \times 10^{57}$ m$^{-6}$. For a plausibility test of this result, we further analyzed the solid state structure of $[Eu(ttham)](ClO_4)_3 \cdot 3H_2O$, from which insight in the organization of the second coordination sphere could be gained. Here the closest non-hydrogen atom was found at a 430 pm distance to the europium ion. This $NH_2$-group of a neighboring complex cation is involved in a strong intermolecular hydrogen-bond to a coordinated carbonyl group. We further restricted the analysis to the 430−600 pm distance range, in which 10−15 heteroatoms ($N_{amide}$, $O_{water}$, $O_{perchlorate}$) are located with respect to the respective europium ion of each of the four independent molecules of the crystal structure. Using these heteroatoms as a first approximation of the number of water molecules comprising the second coordination sphere in solution, $(n_w/r^6)_{cryst}$ ($=\sum_i r_i^{-6}$) was calculated to be $0.67 \times 10^{57}$ m$^{-6}$, averaged over the four independent molecules ($(0.58-0.78) \times 10^{57}$ m$^{-6}$, see Supporting Information, Table S3). The somewhat smaller value compared to that calculated from relaxivity data can be explained by an underestimation of the number of water molecules from the crystal structure data. The amide groups of the next complex cation and the perchlorates, which mainly constitute the second coordination sphere in the crystal structure, are considerably more space-demanding than the dominating water molecules in the solution situation. Taking this into account, as well as the restriction to the 430−600 pm distance range in the solid state analysis, these data convincingly support the results of the above calculation, which in general predicts some 6−47 water molecules in this range (Supporting Information, Table S2).

Finally, using the results of the linear regression analysis, the experimental $r_1$ relaxivity values could be reproduced excellently (open circles in Figure 11A), which made us confident that the chosen model is indeed suitable to describe the dominantly contributing relaxation mechanisms. The relative contribution of the Curie mechanism was found to vary between 8 and 68% (for $Sm^{3+}$ and $Eu^{3+}$, respectively) being generally more important in case of the late lanthanide ions (Figure 11C), whereas the classical dipolar relaxation was more dominant for the earlier lanthanides.

**CEST Experiments.** From their NMR spectra in aqueous solution, exchangeable protons of the ttham complexes could be identified based on the sharpening of their signals at low pH, as reported above. The involvement of these protons in chemical exchange-dependent saturation transfer (CEST) processes was probed by recording their Z spectra at pH 7.4, 310 K, and 7 T (Figure 12A). Depending on the lanthanide ion, peaks were detected between about +80 and −70 ppm.

From these data, the CEST effect, as reported in Figure 12B, was calculated using eq 1. Although this method is commonly used to compensate for contributions from, for example, direct water saturation, it results in a systematic underestimation of the saturation transfer effect for those complexes that possess CEST active protons with MR resonances on both sides of the reference bulk water signal. This artificial reduction of the CEST effect was most prominent in the ttham complexes of the very late lanthanides (Ho−Yb), which exhibited strong Z peaks in the positive and negative saturation frequency offset range that cancel each other substantially. $[Tm(ttham)]^{3+}$, for instance, after presaturation at −42 ppm caused a relative reduction of the bulk water signal of 60% (at 20 mM concentration). According to eq 1, however, a CEST effect of only 30% was calculated, although in this chemical shift range the contribution from direct water saturation is small.

The observed frequencies of the most highly shifted CEST peaks were in excellent agreement with the resonances of the corresponding exchangeable protons as determined from standard $^1$H NMR experiments at pH 2.7 (Figure 12C and Supporting Information, Table S1). In particular for the complexes of the late lanthanides, up to three effective CEST peaks could be distinguished clearly with a chemical shift pattern across the lanthanide series that was in line with earlier experiments using dotam-based ligands.[56]

As shown in Figure 13, the Z spectrum of $[Tm(ttham)]^{3+}$ was compared with those of the Tm complexes of 1bttpam, 4bttpam, and ttha-tm$^{2-}$. The two Z peaks of the ttham complex corresponded with the respective $^1$H NMR peaks of exchangeable protons observed at −42 and −64 ppm (Figure 9A). In addition, a broad shoulder of unresolved Z peaks was observed in the positive chemical shift range up to about +90 ppm, for which no corresponding $^1$H NMR peaks could be observed because of the large line widths. The 1bttpam complex, in comparison, showed similar Z peaks in the negative saturation frequency offset range, but, in addition, relatively sharp signals could also be observed on the positive saturation frequency offset side peaking at chemical shifts of +43 and +59 ppm. Notably two strong peaks of exchangeable protons were observed at identical frequencies in the respective $^1$H NMR spectrum (Figure 9B). This indicated that the positively shifted amide protons associated with the unresolved shoulder in the Z spectrum of $[Tm(ttham)]^{3+}$ were involved in a fast conformational exchange reaction, which in this form did not occur in the respective 1bttpam complex. It was therefore tempting to assign this shoulder to terminal amide groups, whereas the negatively shifted peaks, which were hardly affected by the change of the ligand denticity from 10 to 9, seemed to belong to the 2 central amide groups. From a comparison with the Z spectrum of $[Tm(ttha\text{-}tm)]^+$, which showed two peaks (−32 and −62 ppm) in the negative and also three peaks (+20, +38, +67 ppm) in the positive chemical shift region and which does not comprise central amide groups, it became clear that the situation was more complex, and we

(56) Aime, S.; Barge, A.; Delli Castelli, D.; Fedeli, F.; Mortillaro, A.; Nielsen, F. U.; Terreno, E. *Magn. Reson. Med.* **2002**, *47*, 639–648.

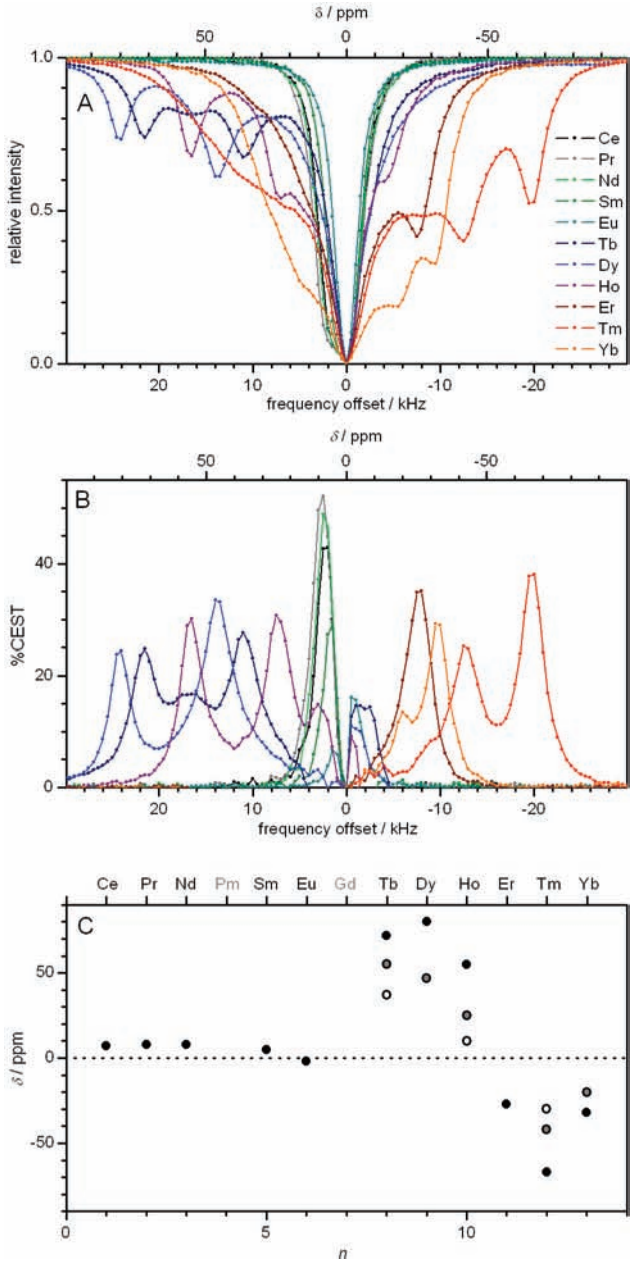


**Figure 12.** Proton Z spectra (A) and thereof calculated CEST spectra (B) of $[Ln(ttham)]^{3+}$ in aqueous solution ($c$([Ln(ttham)]$Cl_3$) = 20 mM, $c$(MOPS) = 10 mM, pH = 7.40, $T$ = 310 K, $B_0$ = 7 T, $B_1$ = 25 $\mu$T, and $t_{sat}$ = 2 s). CEST effect peaks ($\delta_{max}$) as a function of the complexed lanthanide ion ($Ln^{3+}$) as represented by the number $n$ of their 4f electrons (C). The first, second, and third highly shifted peaks are labeled black, dark gray, and light gray, respectively. Chemical shifts ($\delta$) are relative to the resonance frequency of water ($\delta$ = 0 ppm).

therefore did not attempt a further peak assignment. Finally, $[Tm(4bttpam)]^{3+}$, as expected from the multitude of exchangeable proton signals observed in its $^1$H NMR spectrum, did not exhibit well resolved Z peaks.

Next, the Z spectra of $[Tm(ttham)]^{3+}$ and $[Tm(1bttpam)]^{3+}$ were studied as a function of temperature. It was expected that the differences in the solution dynamics of these complexes would impact the temperature dependence of their CEST effect.

In the Z spectra of $[Tm(1bttpam)]^{3+}$ measured at pH 7.4 between 297.5 and 312.5 K (Figure 14A), an intensity increase of the four Z peaks with increasing temperature

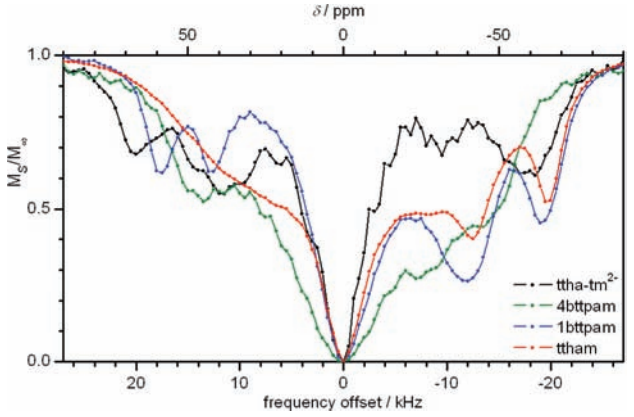


**Figure 13.** Proton Z spectra of $[Tm(L)]^{n+}$ (L = ttham, 1bttpam, 4bttpam, ttha-tm$^{2-}$) in aqueous solution ($c$([Ln(L)]$Cl_n$) = 20 mM, $c$(MOPS) = 10 mM, pH = 7.40, $T$ = 310 K, $B_0$ = 7 T, $B_1$ = 25 $\mu$T, and $t_{sat}$ = 2 s). Chemical shifts ($\delta$) are relative to the resonance frequency of water ($\delta$ = 0 ppm).

was observed in the negative and the positive saturation frequency offset range, which was accompanied by a shift of all peak maxima toward the bulk water resonance. Both effects could be explained as the result of an accelerated proton exchange of the amide groups with the bulk water with increasing temperature, causing the resonance peaks of the two proton pools to broaden and approach each other at the onset of coalescence.[1,2] The change of the calculated effective CEST effect (Figures 14B and C) was surprisingly small at some frequencies (e.g., at −45 ppm), but was very pronounced at a frequency (−63 ppm) at which a significant difference between the two sides of the Z spectrum occurred.

Comparing these results with the temperature-dependent Z spectra of $[Tm(ttham)]^{3+}$ (Figure 15A) similar trends were observed on the negative saturation frequency offset side, whereas the spectral changes were relatively small on the opposite, generally less structured side. A remarkable result of these asymmetric spectral changes was that at one frequency (−45 ppm) an "apparent isosbestic point" was formed, at which a temperature independent CEST effect of 21% could be determined, while at another frequency (−62 ppm) a linear increase of the calculated CEST effect from 0 to more than 40% occurred within the measured temperature range (Figures 15B and C).

In extension of this work, CEST spectra of both complexes, $[Tm(1bttpam)]^{3+}$ (Figure 16) and $[Tm(ttham)]^{3+}$ (Figure 17) were measured at different pH values. Both showed the expected pH-dependence, with a steep increase of the overall CEST-effect between the physiologically relevant pH-values of 6.0 and 7.5. The proton-exchange of coordinated amides is both acid- and base-catalyzed, with the base-catalyzed pathway being generally more effective.[57] Hence, the CEST effect was expected to increase with increasing pH up to a point, at which a further increase was prevented by extensive line broadening of the exchangeable-proton resonances.[11,58] Above pH 8.0, both complexes therefore showed the

(57) McMahon, M. T.; Gilad, A. A.; Zhou, J.; Sun, P. Z.; Bulte, J. W. M.; van Zijl, P. C. M. *Magn. Reson. Med.* **2006**, *55*, 836–847.
(58) Zhang, S.; Michaudet, L.; Burgess, S.; Sherry, A. D. *Angew. Chem., Int. Ed.* **2002**, *41*, 1919–1921.

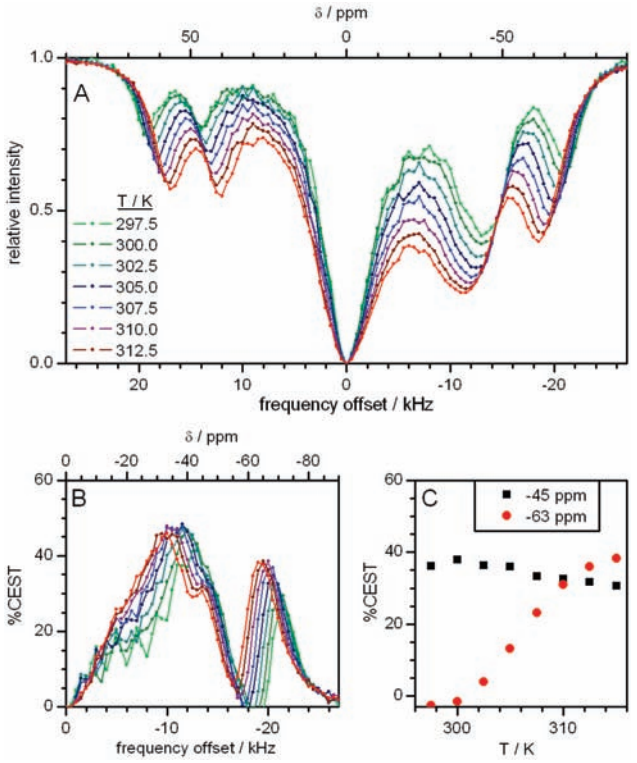


**Figure 14.** Proton Z spectra (A) and thereof calculated CEST spectra (B) of $[Tm(1bttpam)]^{3+}$ in aqueous solution ($c$($[Tm(1bttpam)]Cl_3$) = 20 mM, $c$(MOPS) = 10 mM, pH 7.40, $B_0$ = 7 T, $B_1$ = 25 $\mu$T, and $t_{sat}$ = 2 s) at different temperatures between 297.5 and 312.5 K. CEST effect (%CEST) as a function of temperature (C) at two saturation frequency offsets ($\delta_1$ = −45 ppm (black squares), $\delta_2$ = −63 ppm (red dots)). Chemical shifts ($\delta$) are relative to the resonance frequency of water ($\delta$ = 0 ppm).

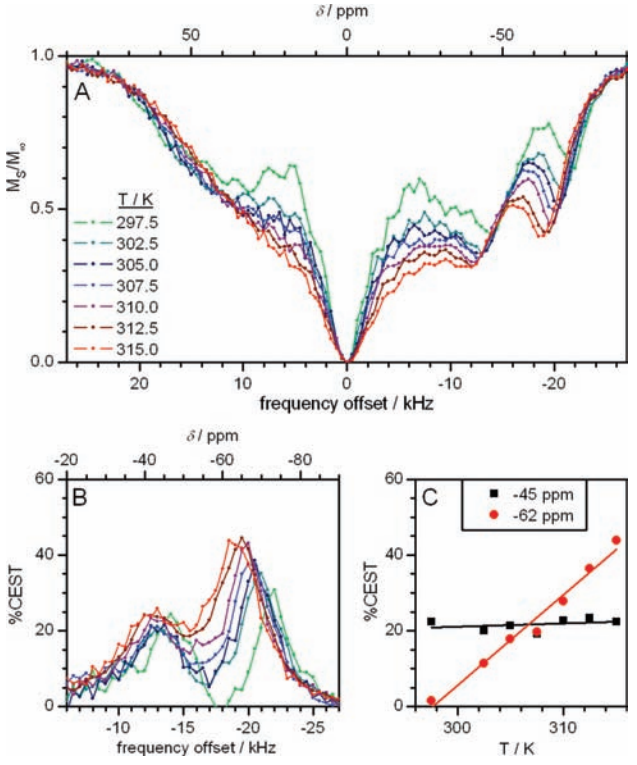


**Figure 15.** Proton Z spectra (A) and thereof calculated CEST spectra (B) of $[Tm(ttham)]^{3+}$ in aqueous solution ($c$($[Tm(ttham)]Cl_3$) = 20 mM, $c$(MOPS) = 10 mM, pH 7.40, $B_0$ = 7 T, $B_1$ = 25 $\mu$T, and $t_{sat}$ = 2 s) at different temperatures between 297.5 and 315.0 K. CEST effect (%CEST) as a function of temperature (C) at two saturation frequency offsets ($\delta_1$ = −45 ppm (black squares), $\delta_2$ = −62 ppm (red dots)). Chemical shifts ($\delta$) are relative to the resonance frequency of water ($\delta$ = 0 ppm).

expected steady decrease of the CEST effect. Depending on the observed frequency, the CEST effect showed a maximum between pH 7.0 and 7.5 ($[Tm(1bttpam)]^{3+}$) or between pH 7.5 and 8.0 ($[Tm(ttham)]^{3+}$). This small difference in the pH dependence may have been caused by varying degrees of cancelation from shift differences of the positive and negative Z peaks, for example, because of slightly different molecular dynamics of the complexes.

In contrast, $[Tm(ttha\text{-}tm)]^{+}$ exhibited a dramatically different pH profile of its Z spectrum. Sharpening and intensity gaining of the Z peaks generally occurred between pH 7 and 8.5, at about +37 ppm even up to pH 9.5 (Figure 18A), before the overall intensity decreased again. The intensity gain up to such high pH values around +37 ppm was most likely the result of a spectral overlap with the peak observed around +65 ppm at pH 8.0, which shifted toward smaller saturation frequency offsets upon pH increase. In parallel, on the negative chemical shift side the Z peak intensity at −57 ppm decreased above pH 8.0. The net result of this complex pH dependence was an increase of the calculated overall CEST effect at +37 ppm from about pH 6.5 up to pH 8.3, followed by a drop at pH 8.8 and a further increase up to pH 10.5. On the negative chemical shift side, however, at −57 ppm a single CEST maximum at pH 8.0 was calculated (Figures 18B and C).

Generally, the peaking of the CEST intensity at a higher pH of about 8.0 as measured at −57 ppm in the case of the monocationic $[Tm(ttha\text{-}tm)]^{+}$ compared with the above two tricationic complexes could be ascribed to their different molecular charges. In principle, a reduction of the effective charge of the complexed thulium(III) ion by the coordination of two acetate groups in the case of the ttha-$tm^{2-}$ ligand could decrease the acidity of the amide protons because of a relative destabilization of the more acidic iminolate resonance form (B, Scheme 2). A similar model had been applied recently to explain electronic substituent effects on the CEST properties of the coordinated water molecule in europium(III) complexes of various dota-tetraamide derivatives.[59] From the kinetic point of view, as discussed above, the amide proton exchange reaction is predominantly base-catalyzed. Coordination of the amide donor to a $Ln^{3+}$ ion imposes a partial positive charge on the amide group (Scheme 2), which, in combination with the overall positive charge of the molecule, repels nearby protons and attracts hydroxide ions to further facilitate the base-catalyzed exchange reaction.[11] A decrease of the overall molecular charge, therefore, resulted in a decrease of the amide proton exchange rate and hence a shift of the maximum CEST effect to higher pH values.

## Discussion

The europium and thulium complexes of the ligands ttham, 1bttpam, 4bttpam, $Bu_2$ttha-tm, and ttha-$tm^{2-}$ (Chart 1) were prepared and their properties were studied in the solid state (all) and in aqueous solution (not $[Ln(Bu_2ttha\text{-}tm)]^{3+}$).

(59) Ratnakar, S. J.; Woods, M.; Lubag, A. J. M.; Kovács, Z.; Sherry, A. D. *J. Am. Chem. Soc.* **2008**, *130*, 6–7.

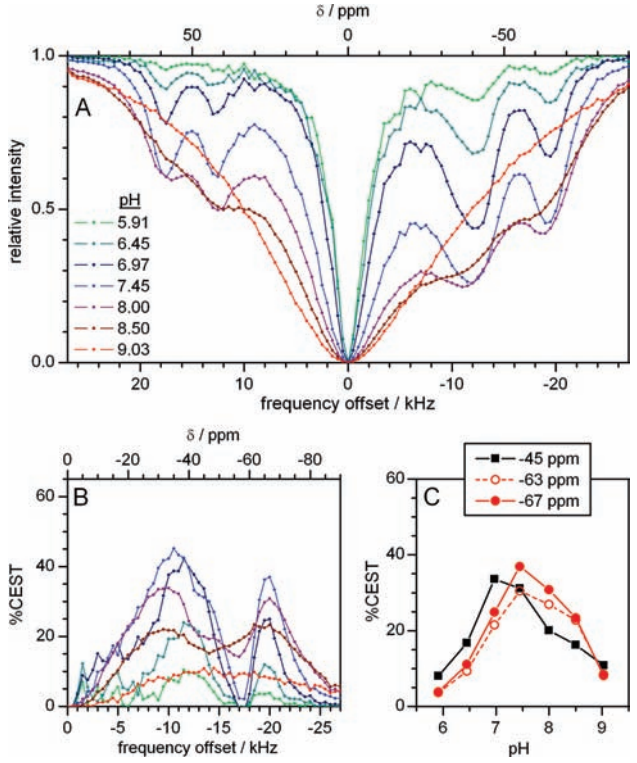


**Figure 16.** Proton Z spectra (A) and thereof calculated CEST spectra (B) of $[Tm(1bttpam)]^{3+}$ in aqueous solution ($c([Tm(1bttpam)]Cl_3)$ = 20 mM, $c$(MOPS) = 10 mM, $T$ = 310 K, $B_0$ = 7 T, $B_1$ = 25 $\mu$T, and $t_{sat}$ = 2 s) at different pH values between pH 5.91 and pH 9.03. CEST effect (%CEST) as a function of pH (C) at three saturation frequency offsets ($\delta_1$ = −45 ppm (black squares), $\delta_2$ = −63 ppm (open red circles), $\delta_3$ = −67 ppm (red dots)). Chemical shifts ($\delta$) are relative to the resonance frequency of water ($\delta$ = 0 ppm).

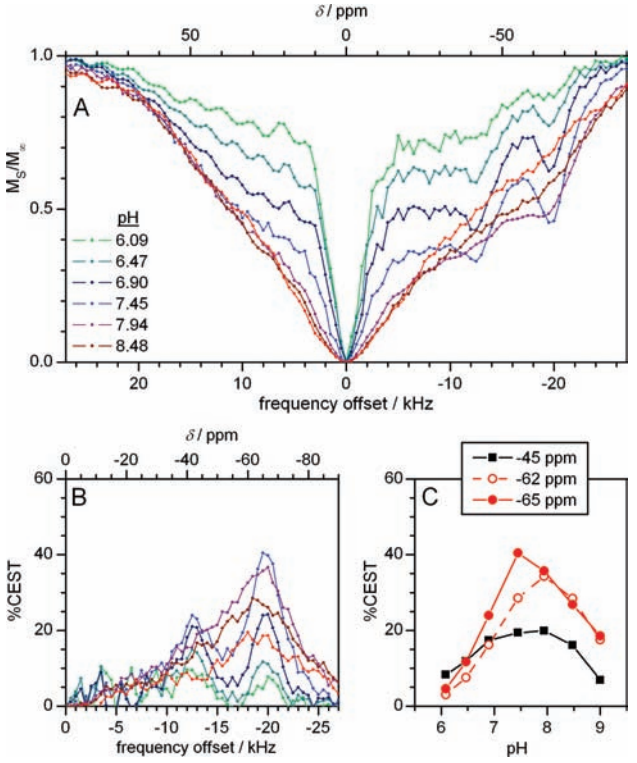


**Figure 17.** Proton Z spectra (A) and thereof calculated CEST spectra (B) of $[Tm(ttham)]^{3+}$ in aqueous solution ($c([Tm(ttham)]Cl_3)$ = 20 mM, $c$(MOPS) = 10 mM, $T$ = 310 K, $B_0$ = 7 T, $B_1$ = 25 $\mu$T for 2 s) at different pH values between pH 6.09 and pH 8.48. CEST effect (%CEST) as a function of pH (C) at three saturation frequency offsets ($\delta_1$ = −45 ppm (black squares), $\delta_2$ = −62 ppm (open red circles), $\delta_3$ = −65 ppm (red dots)). Chemical shifts ($\delta$) are relative to the resonance frequency of water ($\delta$ = 0 ppm).

The ttham ligand, which is the hexaamide derivative of the well studied hexaacetate ligand $ttha^{6-}$, is potentially decadentate providing four tertiary amine and six acetamide donor groups. With the early lanthanide ions $La^{3+}$,[60,61] $Pr^{3+}$,[62] and $Nd^{3+}$,[63−65] the parent $ttha^{6-}$ is known from crystallographic studies to form 10-coordinate complexes. However, in all structurally characterized $ttha^{6-}$-complexes of the later lanthanides starting with $Eu^{3+}$ (Eu,[66] Gd,[67] Tb,[68] Dy,[61,69] Ho,[69,70] Er,[65,69] Yb[71]) one of the four terminal acetate residues remained uncoordinated in the overall 9-coordinate complexes, giving rise to dynamic exchange equilibria between different conformers involving partial decoordination of the ligand.[41] The switch from a 10-fold to a 9-fold coordination is a result of the lanthanide contraction and was therefore expected to also occur within the ttham series.[29,30] On the basis of the evidence provided by a principal component analysis of the respective solid state IR and Raman spectra, this structural change could be concluded to occur moving from $[Er(ttham)]^{3+}$ to $[Tm(ttham)]^{3+}$. Crystallographic analysis confirmed the 10-fold coordination of the respective mononuclear Eu complex and further indicated the presence of substantial first-order steric crowding in its coordination sphere, based on a comparison of the coordinative bond lengths in 10-coordinate $[Eu(ttham)]^{3+}$ and 9-coordinate $[Eu(1bttpam)]^{3+}$ (see Table 3 for an overview of the determined coordination numbers).[28] Metal-binding of the additional tenth donor in the ttham complex forced the average europium-amide distance to increase by some 4 pm compared to the respective 1bttpam complex. In $[Eu(ttha)]^{3-}$, the respective hexaacetate reference complex, the on average another 4 pm shorter europium-acetate bonds ($[Eu(ttha)]^{3-}$: $d$(Eu−O) = 237.1 pm,[66] $[Eu(1bttpam)]^{3+}$: $d$(Eu−N) = 241.3 pm) leave insufficient space to house the tenth donor, forcing the complexes of the $ttha^{3-}$ series to adopt a 9-coordinate structure beginning already with europium. The mixed diacetate-tetraacetamide ligand $ttha\text{-}tm^{2-}$ represents an intermediate case, for which we have provided evidence for a 9-coordinate structure of its mononuclear $Tm^{3+}$ complex, and for a still 10-coordinate structure of the respective $Eu^{3+}$ complex. The further increased steric crowding in the latter complex caused the $Eu^{3+}\rightarrow Eu^{2+}$

(60) Kim, C.-H.; Lee, S.-G. *Bull. Korean Chem. Soc.* **1999**, *20*, 417–421.
(61) Ruloff, R.; Prokop, P.; Sieler, J.; Hoyer, E.; Beyer, L. *Z. Naturforsch.* **1996**, *51b*, 963–968.
(62) Tinant, B.; Bodart, N.; Wullens, H.; Devillers, M. *Z. Kristallogr. NCS* **2002**, *217*, 109–111.
(63) Mondry, A.; Starynowicz, P. *Eur. J. Inorg. Chem.* **2006**, 1859–1867.
(64) Mondry, A.; Starynowicz, P. *Inorg. Chem.* **1997**, *36*, 1176–1180.
(65) Wang, J.; Liu, Z.-R.; Zhang, X.-D.; Jia, W.-G.; Li, H.-F. *J. Mol. Struct.* **2003**, *644*, 29–36.
(66) Wang, J.; Zhang, X. D.; Jia, W. G.; Zhang, Y.; Liu, Z. R. *Russ. J. Coord. Chem.* **2004**, *30*, 130–136.
(67) Ruloff, R.; Gelbrich, T.; Sieler, J.; Hoyer, E.; Beyer, L. *Z. Naturforsch.* **1997**, *52b*, 805–809.
(68) Wang, J.; Liu, X. Z.; Wang, X. F.; Gao, G. R.; Xing, Z. Q.; Zhang, X. D.; Xu, R. *J. Struct. Chem.* **2008**, *49*, 75–83.
(69) Wang, J.; Wang, Y.; Zhang, Z.; Zhang, X.; Liu, X.; Liu, X.; Liu, Z.; Zhang, Y.; Tong, J.; Zhang, P. *J. Coord. Chem.* **2006**, *59*, 295–315.
(70) Mondry, A.; Starynowicz, P. *New J. Chem.* **2000**, *24*, 603–607.
(71) Wang, R.-Y.; Li, J.-R.; Jin, T.-Z.; Xu, G.-X.; Zhou, Z.-Y.; Zhou, X.-G. *Polyhedron* **1997**, *16*, 2037–2040.

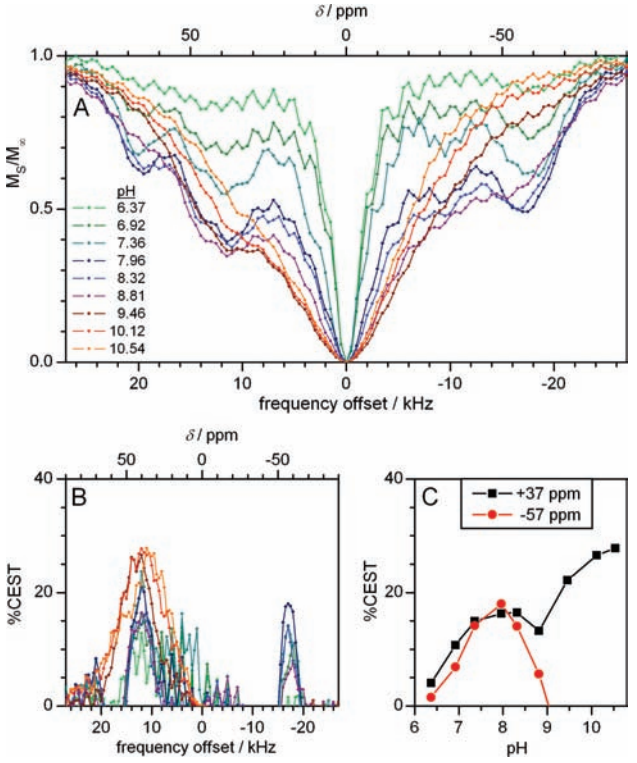


**Figure 18.** Proton Z spectra (A) and thereof calculated CEST spectra (B) of $[Tm(ttha\text{-}tm)]^+$ in aqueous solution ($c$([Tm(ttha-tm)]Cl) = 20 mM, $c$(MOPS) = 10 mM, $T$ = 310 K, $B_0$ = 7 T, $B_1$ = 25 $\mu$T for 2 s) at different pH values between pH 6.37 and pH 10.54. CEST effect (%CEST) as a function of pH (C) at two saturation frequency offsets ($\delta_1$ = +37 ppm (black squares), $\delta_2$ = −57 ppm (red dots)). Chemical shifts ($\delta$) are relative to the resonance frequency of water ($\delta$ = 0 ppm).

**Scheme 2.** Resonance Structures of Coordinated Amide Groups

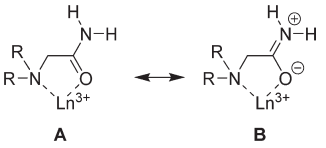


reduction to become electrochemically irreversible, whereas it was still reversible in the respective ttham complex.

The deduced first-order steric crowding is believed to facilitate the fast exchange reaction between conformational isomers of individual complexes in solution. As a result, either more than one subset of NMR resonances was observed, if the exchange between isomers was slow on the NMR time scale, for example, in the case of the 4bttpam complexes, or the NMR signals were found to show extensive line broadening, as seen for most $ttha\text{-}tm^{2-}$ and ttham complexes. A remarkable exception to this general observation were the amide protons of all the said studied ligands. At pH 2.7, where the base-catalyzed exchange reaction of the amide protons with solvent water was sufficiently slow on the NMR time scale, all coordinated ligands exhibited relatively sharp NMR peaks because of the significant contribution of non-line-broadened protons of the bulk water to the overall line width. The LIS of these relatively sharp resonances of the exchangeable protons of the $[Ln(ttham)]^{3+}$ series could therefore be further analyzed. It was confirmed that within the ttham series the switch from a 10-fold to a 9-fold coordination mode, which was deduced for the solid state

**Table 3.** Coordination Numbers of $Eu^{3+}$ and $Tm^{3+}$ Complexes of the Five Studied Ligands in the Solid State and in Solution

| $Ln^{3+}$ | ttham[a] | 1bttpam | 4bttpam | $ttha\text{-}tm^{2-}$ | $Bu_2ttha\text{-}tm$[b] |
|---|---|---|---|---|---|
| $Eu^{3+}$ | 10 | 9 | 9 | 10 | 10 |
| $Tm^{3+}$ | 9 | 9 | 9 | 9 | 10 |

[a] Coordination numbers for Ln = La−Er: 10 and for Ln = Tm−Lu: 9. [b] Determined only in the solid state because of fast hydrolysis in aqueous solution.

to occur upon moving from the Er to the Tm complex, also occurred between these two metals in solution.

The complexes $[Tm(L)]^{n+}$ ($n$ = 1 or 3) of the above ligands, which did not bear a water molecule in the first coordination sphere, were used to evaluate the influence of the ligand on their proton longitudinal relaxivity. The observed relaxivity increase according to 1bttpam < ttham ∼ $ttha\text{-}tm^{2-}$ < 4bttpam is consistent with earlier reports on the relaxivity of respective ytterbium complexes and could be related to a combination of steric and dynamic effects that determined the interaction of solvent water molecules with the encapsulated lanthanide ion.[23] It could be concluded that in these 9-coordinate, oligoamide complexes a relatively high relaxivity was supported primarily by a high conformational flexibility, which could in part be compensated for by providing a tenth donor group that remains uncoordinated on average. From an analysis of the variation of the longitudinal relaxivity within the ttham series of lanthanide complexes, we inferred the relaxivity to be dominated by second coordination sphere interactions, with an ascendant contribution of the classical dipolar relaxation mechanism for the earlier (Ce−Sm) and very late (Tm, Yb) lanthanides, and a prevailing Curie relaxation mechanism for most of the remaining paramagnetic lanthanide ions.

The above complexes were designed with the aim to provide a high number of CEST-active amide groups per lanthanide ion, which, in combination with a low relaxivity due to the simultaneous exclusion of water molecules from the first coordination sphere, promised high overall CEST effects. With the earlier studied $[Yb(ttham)]^{3+}$ complexes this was only partially achieved because of the low symmetry of these coordinatively frustrated 9-coordinate compounds.[23] Nevertheless, even though 10-coordinate ttham complexes with an approximate $C_2$ symmetry have now been obtained for the lanthanides La−Er, the CEST activity remained spread over numerous peaks in a relatively wide chemical shift range, preventing the realization of very high CEST effects in a small frequency range. The lower symmetry of the ttham complexes is therefore a shortcoming compared to the better studied complexes of various dotam (dotam = 1,4,7,10-tetraazacyclododecane-1,4,7,10-tetraacetamide) derivatives, which force the exchangeable protons to adopt symmetry-equivalent positions in those generally $C_4$-symmetric complexes, hence exhibiting few proton resonance peaks in a very narrow chemical shift range.[8,56,72]

As a result of the coordinative frustration and flexibility of $[Yb(ttham)]^{3+}$, its $^1H$ NMR spectrum had been found to show a strong temperature dependence because of coalescence effects between 293 and 353 K.[23] $[Tm(ttham)]^{3+}$, the left neighbor in the lanthanide series, according to the above

(72) Burdinski, D.; Lub, J.; Pikkemaat, J. A.; Langereis, S.; Grüll, H.; ten Hoeve, W. *Chem. Biodiversity* **2008**, *5*, 1505–1512.

is still sufficiently crowded in the first coordination sphere to prevent binding of the tenth amide donor. Nevertheless, the binding of the tenth donor became thermodynamically favorable already for the second next neighbor, [Er(ttham)]$^{3+}$. The 9-coordinate Tm complex was therefore expected to exhibit interesting temperature-dependent CEST properties. The observed peculiar asymmetry of its Z spectrum, with well-defined and extensively broadened peaks in the negative and positive chemical shift range, respectively, resulted in the formation of an "apparent isosbestic point" at −45 ppm in the series of CEST spectra recorded at different temperatures. Simultaneously at −62 ppm the CEST effect increased linearly from 0 to more than 40% between 297.5 and 315 K under said conditions. This situation is ideal for CEST-based temperature mapping, allowing for a temperature-independent determination of the concentration of the CEST agent at one frequency and a quantification of the absolute temperature at a second frequency, while benefitting from a linear calibration curve.[10,14,73,74]

The huge potential of CEST CAs also as efficient pH reporters, because of the strong pH dependence of the CEST effect, has been widely recognized.[13,56,58] This makes them attractive for the imaging of pathologies that are characterized by alterations in the tissue pH, such as cancer or atherosclerosis.[75−77] The CEST spectra of [Tm(1bttpam)]$^{3+}$ and [Tm(ttham)]$^{3+}$ exhibited an expected pH-dependence, with a steep increase of the overall CEST effect between the physiologically relevant pH-values of about 6.0 and about 7.5, followed by an expected decrease above pH 8.0. It is particularly remarkable that in [Tm(ttham)]$^{3+}$ the strongly pH-dependent CEST effect is temperature-independent at the same time, allowing for an effective decoupling of these important physiological parameters and, in principle, a simultaneous temperature and pH mapping using a suitable ratiometric approach.[78]

To reduce the unfavorable osmotic impact of such typically tricationic lanthanide amides in *in vivo* applications, it is a common strategy to substitute one of the two protons of the amide donor group with an anionic residue, often a methylene carboxylate or a methylene phosphonate group, which typically has little influence on the pH dependence of the CEST effect.[12,58,79] Following a slightly different approach, we replaced the two central of the six acetamide donors of the ttham ligand with acetic acid groups providing eventually the monocationic complex [Tm(ttha-tm)]$^{+}$. Compared with the above mentioned tricationic Tm complexes, [Tm(ttha-tm)]$^{+}$ exhibited a remarkably different CEST pH profile with the highest CEST effects being shifted toward significantly higher pH values, which could be explained by a $\pi$-interaction of the negative charge of the acetate donors with the amide groups.

## Conclusion

Overall 21 new mononuclear lanthanide complexes were prepared, to obtain improved paraCEST CAs for MRI. The five used nona- or decadentate ligands, ttham, 1bttpam, 4bttpam, $Bu_2$ttha-tm, and ttha-tm$^{2-}$, of which the latter two were newly synthesized, were designed to fully saturate the first coordination sphere of the encapsulated lanthanide ions and to provide up to 12 CEST-active amide protons per molecule. Within the series of ttham lanthanide complexes, the coordination mode changed from 10-coordinate to 9-coordinate moving from [Er(ttham)]$^{3+}$ to [Tm(ttham)]$^{3+}$ in the solid state, as well as in solution, because of the lanthanide contraction effect. The dangling amide group of the 9-coordinate Tm to Lu complexes caused these asymmetric complexes to exhibit dynamic conformational changes in solution. As a result, CEST effects were lower than expected. On the other hand, in particular the CEST effect of the Tm complex showed a very interesting temperature- and pH-dependence, which opened the opportunity for simultaneous temperature and pH mapping using a ratiometric CEST approach. The studied variation of the ligand structural motif led to the conclusion that even small modifications can have a dramatic impact on the CEST properties of the respective complexes, in particular, if those complexes start to behave dynamically because of the presence of excessive steric crowding.

**Acknowledgment.** We are grateful to Holger Grüll and Sander Langereis (Philips Research) for helpful discussions. Cesar Diez (Philips Research) and Henk-Jan Verhoef (Syncom b.v.) are acknowledged for synthesis support. We thank our colleagues Danielle Beelen and Séverine Girard for NMR measurements, Piet Rommers for potentiometric measurements, and Thea Haex, Jeanette Smulders, Carry Hermans, and Adrie Jonkers (all Philips Research) for elemental analyses. Financial support by the Dutch government (Project code: BSIK 03033 "Molecular Imaging of Ischemic Heart Disease") is gratefully acknowledged.

**Supporting Information Available:** Detailed crystallographic data for three structures in CIF form. $^1$H NMR spectra of complexes [Ln(ttham)]$^{3+}$ (Ln = La, Ce, Pr, Nd, Sm, Tb, Dy, Ho, Er, Lu) at pH 7.40 and 2.70 (Figures S1−S5). Observed chemical shift ($\delta$) and LIS ($\delta'$) of the most highly shifted amide protons of the complexes [Ln(ttham)]$^{3+}$ (Ln = Ce−Yb, except Pm) in aqueous buffer solution tabulated (Table S1) and plotted as $\delta'/C^D$ versus $\langle S_Z\rangle/C^D$ (Figure S6). Details of the linear regression according to eq 11 (Equations S1−S3, Table S2). Europium−heteroatom distances in the 430−600 pm range in the crystal structure of [Eu(ttham)](ClO$_4$)$_3\cdot$3H$_2$O. This material is available free of charge via the Internet at http://pubs.acs.org.

(73) Li, A. X.; Wojciechowski, F.; Suchy, M.; Jones, C. K.; Hudson, R. H. E.; Menon, R. S.; Bartha, R. *Magn. Reson. Med.* **2008**, *59*, 374–381.
(74) Terreno, E.; Delli Castelli, D.; Cravotto, G.; Milone, L.; Aime, S. *Invest. Radiol.* **2004**, *39*, 235–243.
(75) Pérez-Mayoral, E.; Negri, V.; Soler-Padrós, J.; Cerdán, S.; Ballesteros, P. *Eur. J. Rad.* **2008**, *67*, 453–458.
(76) Gillies, R. J.; Raghunand, N.; Garcia-Martin, M. L.; Gatenby, R. A. *IEEE Eng. Med. Biol. Mag.* **2004**, *23*, 57–64.
(77) Naghavi, M.; John, R.; Naguib, S.; Siadaty, M. S.; Grasu, R.; Kurian, K. C.; van Winkle, W. B.; Soller, B.; Litovsky, S.; Madjid, M.; Willerson, J. T.; Casscells, W. *Atherosclerosis* **2002**, *164*, 27–35.
(78) Wegh, R. T., Pikkemaat, J. A., Willard, N. P. Method for using CEST contrast agents in MRI. U.S. Patent US2008/0188738.
(79) Woods, M.; Caravan, P.; Geraldes, C. F. G. C.; Greenfield, M. T.; Kiefer, G. E.; Lin, M.; McMillan, K.; Prata, M. I. M.; Santos, A. C.; Sun, X.; Wang, J.; Zhang, S.; Zhao, P.; Sherry, A. D. *Invest. Radiol.* **2008**, *43*, 861–870.